Probabilistic Machine Learning for preventing fatigue failures in Additively Manufactured SS316L

Engineering Failure Analysis 168 (2025) 109081

Contents lists available at ScienceDirect

Engineering Failure Analysis

journal homepage: www.elsevier.com/locate/engfailanal

Probabilistic Machine Learning for preventing fatigue failures in Additively Manufactured SS316L

Alessio Centola *, Alberto Ciampaglia, Davide Salvatore Paolino, Andrea Tridello

Politecnico di Torino, Department of Mechanical and Aerospace Engineering, Torino 10129, Italy

ARTICLE INFO

Keywords:
Fatigue
Probabilistic machine learning
Machine learning
Process parameters
Design
Additive manufacturing
SS316L
Failure prevention

ABSTRACT

This study presents a probabilistic machine learning approach to predict and improve the fatigue performance of additively manufactured SS316L components. By analyzing key manufacturing parameters as process settings, thermal treatments and surface treatments, the developed models provide statistical estimations of fatigue strength, that provides valuable insights to extend fatigue life. Trained on an experimental database of fatigue tests, the Bayesian Neural Network (BNN) is employed to separate model uncertainty, related to data limitations, from the uncertainty inherent in the fatigue phenomenon. This approach robustly predicts Probabilistic Stress-Life (PSN) curves, offering valuable insights into the impact of manufacturing parameters on fatigue resistance, allowing to further postpone fatigue failures. The results demonstrate increased robustness and trustworthiness compared to other deterministic machine learning models, making this method suitable for critical applications where failure prevention is crucial.

1. Introduction

Additive manufacturing (AM) is an emerging production process redefining the landscape of modern engineering, with Powder Bed Fusion – Laser Beam (PBF-LB) being a paramount technology in producing lightweight metal components with optimized geometries.

Abbreviations: AM, Additive Manufacturing; BNN, Bayesian Neural Network; C90, Confidence level at 90%; CDF, Cumulative distribution function; E_d, Volumetric energy density; $_f$, failure; FFNN, Feed-Forward Neural Network; FFNN-L, Feed-Forward Neural Network Likelihood; h, Hatch Distance [μm]; HCF, High Cycle Fatigue; HIP, Hot Isostatic Pressing Thermal Treatment; LOF, Lack of fusion; LPBF, Laser power bed fusion; m, R50 curve slope coefficient; ML, Machine Learning; MLLE, Maximum Log-Likelihood Estimate; $MLLE_f$, Maximum log-likelihood estimate of a failure; $MLLE_r$, Maximum log-likelihood estimate of a runout; MSE, Mean squared error; N_f, Number of cycles to failure; NLL, negative log-likelihood; NN, Neural Network; N_r, Number of cycles of a runout specimen; P, Laser Power [W]; PBF-LB, Powder Bed Fusion – Laser Beam; PDF, Probability density function; PINN, Physics Informed Neural Network; PP, Process Parameters; PSN, Probabilistic Stress-Life (Curves); q, R50 intercept coefficient; q_{R90C90}, R90C90 intercept coefficient; $_r$, runout; R90, Reliability level at 90%; ReLU, Rectified linear unit activation function; R_f, Runout flag; S_a, Applied stress amplitude [MPa]; SN, Stress-life curves; SS316L, Stainless Steel 316L; ST, Surface Treatment; ST_DN, Deep Nitriding surface treatment boolean; ST_EP, Electro-polishing surface treatment boolean; ST_Grind, Grinding surface treatment boolean; ST_Mac, Machining surface treatment boolean; ST_Nitr, Nitriding surface treatment boolean; ST_Pol, Polishing surface treatment boolean; ST_SSP, Severe Shock Peening surface treatment boolean; ST_VF, Vibratory Finishing surface treatment boolean; t, Layer Thickness [μm]; T, Thermal Treatment Temperature [°C]; tanh, Hyperbolic tangent activation function; TDB, Training Database; TT, Thermal Treatment; TT_Ann, Annealing (Stress relief) thermal treatment boolean; TT_HIP, Hot isostatic pressing thermal treatment boolean; v, Laser Scan Speed [mm/s]; VHCF, Very High Cycle Fatigue; V_{risk}, Risk Volume; Δt, Thermal Treatment Time [hours]; ϑ, Building Orientation [°]; ρ_{rel}, Relative density [%]; σ, Dataset standard deviation.

* Corresponding author.
E-mail address: alessio.centola@polito.it (A. Centola).

https://doi.org/10.1016/j.engfailanal.2024.109081
Received 12 September 2024; Received in revised form 28 October 2024; Accepted 13 November 2024
Available online 19 November 2024

Another major benefit is that additive manufacturing processes enable the production of complex shapes and geometries, tailored and customized for the specific application. Among the various metals used in AM, stainless steel 316L (SS316L) is particularly valued for its versatility, strength, and corrosion resistance. Although PBF-LB SS316L parts have excellent static mechanical properties, their fatigue performance is worse than that of parts made using conventional manufacturing processes. Among the factors that impact fatigue performance, process parameters (PP) have been observed to play a fundamental role. The reduced fatigue performance of as-built PBF-LB SS316L components is largely due to defects arising during the layer-by-layer manufacturing process [1]. These defects, such as porosities and lack of fusions (LOFs), are preferential nucleation sites for fatigue cracks [2]. The material microstructure is also influenced by the combination of these PP, since the local thermal history can alter the microstructure of the grains [3] and subsequently affect fatigue performance [4]. Therefore, optimizing the combination of PP is fundamental to creating components with the highest relative density (ρ_{rel}) and the lowest porosity. Similarly, post-processing treatments can affect the fatigue response. For example, thermal treatments (TT) like hot isostatic pressing (HIP) can reduce the size of manufacturing defects. Another common TT is a stress relief treatment, which, if carefully designed in terms of heating temperature and time, has been shown to improve the fatigue response of PBF-LB parts by reducing detrimental residual stresses that may originate during the PBF-LB process [5,6]. A fundamental role is played by surface treatments (ST), like machining, polishing and nitriding, which can enhance the surface quality by reducing the roughness, consequently reducing the number of surface defects, which are critical in the high cycle fatigue (HCF) regimen. These treatments positively affect the fatigue response since surface defects lead to a lower fatigue limit with respect to internal defects [7]. The assessment of PP, TT, and ST on the fatigue response would permit to manufacture PBF-LB parts with optimized and enhanced fatigue response. However, due to the large number of parameters involved and their interactions, this is rather complex for economic reasons and would require a not feasible number of experimental tests. Indeed, the above-described parameters also interact with each other, making it quite impossible to define a model which provides in output the fatigue response starting from PP, TT and ST, even with optimized design of experiments (DOEs) strategies [8]. It must be noted that many results are available and spread in the literature, obtained by varying specific manufacturing parameters, thus not providing a global insight on the fatigue response and the fatigue behavior of AM parts. The large variability of the fatigue results further complicates the analysis of the fatigue response and the assessment of the influence of the manufacturing parameters. On the other hand, with large datasets available in the literature, complex relationships between numerous factors can be reliably managed with Machine Learning (ML) techniques. Indeed, existing literature datasets can be leveraged to train the ML model, enabling researchers to exploit the extensive test campaigns already carried out, while thoroughly mapping the relationships between a component fatigue life and the aforementioned factors. Among several ML architectures, Neural Networks (NN) are one of the most flexible, efficient, and widespread. Indeed, NN can be thought of as a universal approximator, though they are often mistakenly compared to the human brain, allowing to handle multivariate problems with ease. The use of NN for the assessment of the fatigue life of AMed parts is a relatively young research field.

Over the past five years, there has been a noticeable increase in ML studies focusing on the fatigue response of various PBF-LB materials [9]. This surge in interest reflects a growing recognition of the potential benefits that ML can offer in optimizing AM processes and improving the fatigue performance [10]. Different types of NNs have been employed for this task. In particular, Feed-Forward Neural Networks (FFNN) have proven to be reliable candidates to model the link between manufacturing process and fatigue performance. Centola et al. [11] employed a FFNN trained with literature data to predict the fatigue life of Ti6Al4V alloy based on PP, TT and ST conditions. Tridello et al. [12] developed two FFNN to evaluate critical defects in PBF-LBed AlSi10Mg and Ti6Al4V alloys. The model could accurately predict the distribution of the critical defects described with a Largest Extreme Value Distribution, estimated with the FFNN. Bagherifard et al. [13] conducted tests on PBF-LBed AlSi10Mg V-notched specimens to develop a FFNN that correlates residual stress, hardness, and roughness to the fatigue life of specimens. Dang et al. [14] proposed a properly designed FFNN to estimate the fatigue performance from fractography analyses. Hornas et al. [15] developed a FFNN to address the impact of defects, detected via micro-computed tomography, and stress amplitude on the fatigue performance of PBF-LBed Ti6Al4V. Zhang et al. [16] developed a ML framework that combines two FFNNs, respectively fed with PPs and static properties, to forecast the fatigue performance of PBF-LBed SS316L samples using both experimental and literature data.

Complex engineering phenomena, like fatigue of AMed parts, however, can be better forecast through ML algorithms embedding previous physical knowledge, such as physics-informed neural networks (PINN). These NNs adopt prior engineering knowledge to design a constrained loss function that leverages physical formulas. In this way, the obtained results approach a more realistic outcome that likely benefits the model generalization. In [11], a PINN has been created to improve the predictions of (stress-life) S-N curves by penalizing monotonically increasing predictions of the S-N curves, which may result when using FFNN. Ciampaglia et al. developed a PINN environment to link the PP and TT parameters with the fatigue response of AlSi10Mg [17] and Ti6Al4V [18] samples. The model architecture leverages the Murakami formulation to link the input features and is trained on the available literature data. Salvati et al. [19] fine-tuned a PINN to predict the life of defective AlSi10Mg coupons by incorporating linear elastic fracture mechanics formulations. The results presented in the above-mentioned articles marked a shift to innovative data-centric methodologies that encompass data-science methods and physics-based formulations. However, these methodologies give a deterministic description of the fatigue response, while its intrinsic stochastic nature fosters the need for statistical methodologies to assess the aleatoric response of the parts [20]. In the present paper, the ML models are declined in a probabilistic version, to model the stochastic nature of the fatigue response.

Chen and Liu [21] developed a PINN to predict the fatigue life of small datasets, while properly treating runout specimens thus providing statistical confidence intervals for the predicted Probabilistic S-N (PSN) curves. This has been accomplished by adopting a properly designed loss function that is equal to the negative maximum log-likelihood estimate (MLLE). In this way, the PINN minimizes during training this custom loss function to provide prediction with aleatoric confidence intervals.

To the best of the authors' knowledge, this is the only article presenting an application of a probabilistic ML method in this field.

It is important to note that probabilistic approaches should properly consider the two main sources of uncertainty related to a

model prediction: (i) the aleatoric uncertainty, defined as the intrinsic scatter of the fatigue phenomena; (ii) the epistemic uncertainty, defined as the confidence of the prediction which is related to the model (i.e., the ML model in this case). The first has been extensively discussed in the literature, and a large variety of statistical approaches can be used to assess the fatigue response at different reliability levels. Methodologies which consider the uncertainty of the ML model instead are recent in the literature, and their application to fatigue problems is fundamental to preserve a clear distinction between the aleatoric and epistemic uncertainty.

The focus of the present work is to develop NN models that can model the aleatoric uncertainty intrinsic to the fatigue phenomenon, as well as the ML model uncertainty (i.e., the epistemic uncertainty) and to separate their contribution. The developed NN algorithms can predict the PSN curves that can be used to safely design AMed parts. First, an FFNN is developed to predict the parameters of a linear S-N curve with normally distributed data (FFNN-L); then, a PINN is introduced to predict the above-mentioned parameters (PINN-L); last, a Bayesian Neural Network (BNN) is developed to predict the R90C90 (i.e., 90 % reliability and 90 % confidence level) curves defined with the Owen's method [22], to finally separate the experimental uncertainty from the ML model one. These algorithms have been trained on a training database (TDB) and validated by considering literature data.

2. Experimental data and fatigue models

This section describes the data used to train the proposed ML models, which include manufacturing information about the additive process and experimental fatigue tests results. Thereafter, the empirical fatigue models, which will be integrated with the ML algorithms described in Section 3, are briefly introduced and applied to the collected data. The ML models employed in this study, are proposed to leverage well-established and accepted fatigue design models, while ensuring that the ML models infer the associated statistical uncertainty associated with the training data and dataset evaluation.

2.1. Database

This section discusses the parameters used for the training of the developed NN algorithms. Creating a fully populated TDB is crucial for the ML algorithms, which should contain comprehensive data. In ML terminology, the inputs are called features (x_i), and the outputs to be predicted are called labels (y_i). The goal of the proposed ML approaches is to predict the fatigue PSN curves of PBF-LB SS316L components based on various process parameters. Given that the fatigue characteristics of this alloy are strongly influenced by the defect distribution, to have good predictive accuracy, PP, TT and ST are included, as explained below. It is crucial to carefully select the NN features to accurately forecast the fatigue response. During the PBF-LB process, a laser melts metal powders layer by layer on a building platform. The layer thickness t is determined by the space travelled by the platform after each deposition. The orientation of the part on the platform, referred to as the building orientation ϑ, impacts the final product mechanical properties, with common angles being horizontal (0°), vertical (90°), and inclined (45°). Other key parameters include the hatch distance h, which is the spacing between successive laser passes, the laser power P, and the laser scan speed v. If h is too large, the particles might not be fully melted, while small hatch may lead to multiple meltings of the same portion of material [23,24]. Similarly, high v with low P might lead to incomplete melting, while high P with low v may cause over-melting and affect part quality [23,25]. Similarly, *TT*, such as annealing (*Ann*) and *HIP*, can significantly impact the fatigue response [26], when proper temperatures (T) and duration (Δt) are correctly defined. These are therefore considered as features for the developed NN. PBF-LB SS316L specimens commonly undergo an *Ann* which consists of reheating components at a temperature (500 °C to 1050 °C) below the melting point to reduce residual thermal stresses generated during the manufacturing process. ST also affect fatigue response. Due to poor surface finishes in AMed parts, processes like machining (*ST_Mac*), polishing (*ST_Pol*), electro-polishing (*ST_EP*), grinding (*ST_Grind*), severe shock peening (*ST_SSP*), vibratory finishing (*ST_VF*), nitriding (*ST_Nitr*), and deep nitriding (*ST_DN*) are also used to improve the surface quality and, consequently, the fatigue performance. These ST are also considered as boolean features for the NN to improve the accuracy of the predictions. The literature has been thoroughly searched to gather as much training data as possible. Despite the limited data availability, the TDB includes a broad range of key PP, TT, and ST. To overcome this limitation, the BNN has been purposely employed to manage uncertainty and provide reliable predictions.

It should be noted that only those articles reporting the process parameters P, v, t, h, and ϑ, along with information about thermal and surface treatments, are considered. Information about the AM machine and the powder used to produce the specimens was intended to be included, as it is well known that processing parameters can vary between different AM machines, affecting material properties. However, only a few of the datasets provided this information. To maintain consistency in the TDB and maximize the number of training points, it has been decided not to include machine-specific details. For each failure or runout event, the stress amplitude S_a and the corresponding number of cycles N_f are included, along with a boolean runout flag R_f, to denote whether the point is a failure ($R_f = 0$) or a runout ($R_f = 1$). The fatigue lifetime range below 10^7 cycles was considered due to limitations in the available training data from literature sources. Therefore, the Very High Cycle Fatigue (VHCF) regime was not explicitly modeled and considered in this analysis, due to the limited data points in this region. However, the developed machine learning framework is capable of modeling the fatigue behavior in the VHCF regimes as well, but additional data covering this life range should be available. The fatigue tests reported in the literature are primarily conducted in three configurations: rotating bending (i.e., stress ratio $R = -1$), pulsating tensile and bending (i.e., $R \neq 0$). To compare data with different stress ratio, the Smith-Watson-Topper correction is applied ($S_{a,R=-1} = S_{max} \bullet \sqrt{0.5 \bullet (1 - R)}$), allowing the calculation of equivalent stress amplitude at $R = -1$. To account for the scale effect, which can greatly affect the fatigue response, the risk volume V_{risk} is calculated according to the testing configuration and specimen geometry. As detailed in [7], V_{risk} corresponds to the material volume that undergoes 90 % of the nominal stress. In the training

database, *TT*, *ST* and R_f are denoted as Boolean features using the one-hot encoding strategy, where 1 stands for true and 0 for false. When it comes to *T*, 20 °C was set as the default for cases where the TT is not applied (both *TT_Ann* and *TT_HIP* = 0). The same reasoning applies for Δt, with 0 h when a TT is not performed. Diverse ranges of *T* and Δt are found in the literature and are reported as such in case one of the two TT is performed.

In this work, N_f is the dependent variable and S_a the independent one. This interpretation mirrors actual fatigue testing, where S_a is predetermined, and the cycles to failure are then measured. Unlike in [11], information concerning runout specimens is properly treated thanks to R_f, considering the correct statistical formulation. A summary of the data used to train the ML algorithms is presented in Table 1, comprising 518 fatigue points from 51 datasets extrapolated from 17 articles. For brevity, the S_a, N_f and R_f columns are removed just to report the *PP*, *TT*, *ST* and V_{risk}. The amount of data of each dataset is different, with some having just one point per stress amplitude level. Despite this, datasets with a single stress amplitude level are retained since they could be supplemented with similar datasets.

2.2. Linear fatigue model with constant normal distribution

The HCF response of metallic materials is generally described by power law function, commonly referred to as Basquin's law. A statistical variation of the model can be obtained assuming a normal distribution of the fatigue life [44]. This method will be referred to as "linear model" in the following. N_f is a random variable with its mean that linearly varies with the applied stress amplitude S_a, and a constant standard deviation σ. The cumulative distribution function (CDF) of N_f, can be then found in Eq. (1):

$$CDF_{\log_{10}(N_f)} = \phi\left(\frac{\log_{10}(N_f) - (m \bullet \log_{10}(S_a) + q)}{\sigma}\right), \tag{1}$$

with the slope *m*, the intercept *q* and the standard deviation σ assumed to be constant, and to be estimated by considering the experimental data. For each dataset, the parameters are estimated by minimizing the negative log-likelihood function (NLL), reported in Eq. (2):

$$\begin{cases} NLL = -(MLLE_f + MLLE_r) \\ MLLE_f = \sum_i^M (1 - F_{r,i}) \bullet \ln\left(PDF\left(\log_{10}(N_{f,i}) \,|m \bullet \log_{10}(S_{a,i}) + q; \sigma\right)\right) \\ MLLE_r = \sum_i^M F_{r,i} \bullet \ln\left(1 - CDF\left(\log_{10}(N_{r,i}) \,|m \bullet \log_{10}(S_{a,i}) + q; \sigma\right)\right) \end{cases}, \tag{2}$$

where *M* is the number of specimens for the considered dataset and the subscripts *f* and *r* stand for failure and runout, respectively. $R_{f,i}$ is the runout flag for the *i*-th specimen, PDF is the probability density function [22]. For each dataset, once the constant coefficients are estimated, the PSN curves at the selected reliability levels can be estimated.

2.3. Reliability bounds and confidence intervals

The statistical models provide an estimate of the fatigue life with a variability imputable, for example, to the presence of microstructural irregularities (e.g., defects), which act as root cause. In the design of engineering structures, fatigue curves at a defined reliability and confidence levels (e.g. R90C90 curve) are used, rather than P-S-N curves with a specific high level of reliability. In the following, according to a standard notation, the R90 PSN curve indicates the 10th percentile PSN curve. While the concept of reliability is related to the aleatoric uncertainty for fatigue, the concept of confidence is introduced to handle epistemic uncertainty. The epistemic uncertainty is related to the model parameter estimation. In essence, the R90 curve at a 90 % confidence level (R90C90) provides the P-S-N curve estimated according to the considered fitting model (e.g., the Basquin model) which lies below the 90 % of the R90 curves obtained with different subsets. In this study, the R90C90 curve was selected as an example to strike a balance between safety and conservative designs, but the model can be adjusted to accommodate any desired combination of reliability and confidence levels (e.g., R95C95, R90C95) depending on the specific design requirements.

In the literature and in industrial applications, the R90C90 PSN curves are commonly estimated with the Owen's method [22], which requires shifting leftward the R50 linear curve by a factor k_{Owen} multiplied by the fatigue life standard deviation. The R90C90 curve results into a linear curve with slope m_{R90C90} equal to the R50 curve slope *m*, whereas the intercept q_{R90C90} is calculated according to Eq. (3):

$$q_{R90C90} = q - k_{Owen} \bullet \sigma, \tag{3}$$

where *q* is the R50 curve intercept obtained from Eq. (2), σ is the dataset standard deviation and k_{Owen} is a multiplicative coefficient obtainable from [22]. The linear model and the R90C90 PSN curves have been estimated to properly train the developed ML algorithms and to separate and investigate the contribution of the aleatoric and epistemic uncertainty. It is worth noting that, typically, the Owen method is used for estimating R90C90 curves, with this estimation relying on experimental data obtained under specific AM production conditions. The method proposed in the article, on the other hand, can estimate the design curves with good approximation

Table 1
SS316L Training Database used to train the Neural Networks.

Code	Ref	ϑ	P	v	h	t	V_{risk}	T	Δt	TT_Ann	TT_HIP	ST_Mac	ST_Pol	ST_EP	ST_Grind	ST_SSP	ST_VF	ST_Nitr	ST_DN
0	[27]	90	103	425	130	30	28.9	20	0	0	0	0	0	0	0	0	0	0	0
1		90	103	425	130	30	28.9	20	0	0	0	1	0	0	0	0	0	0	0
2		90	103	425	130	30	28.9	20	0	0	0	1	1	0	0	0	0	0	0
3	[28]	0	350	1000	100	30	173	20	0	0	0	1	1	0	0	0	0	0	0
4		90	350	1000	100	30	173	20	0	0	0	1	1	0	0	0	0	0	0
5		45	350	1000	100	30	173	20	0	0	0	1	1	0	0	0	0	0	0
6		90	350	1000	100	30	173	20	0	0	0	0	0	0	0	0	0	0	0
7		45	350	1000	100	30	173	20	0	0	0	0	0	0	0	0	0	0	0
8	[29]	0	250	800	100	50	81.2	20	0	0	0	1	1	0	0	0	0	1	0
9		0	250	800	100	50	81.2	20	0	0	0	1	1	0	0	0	0	0	1
10	[30]	90	190	750	120	30	603	20	0	0	0	0	1	0	0	0	0	0	0
11		90	190	750	120	30	603	20	0	0	0	1	1	0	0	0	0	0	0
12		90	190	750	120	30	603	900	2	1	0	0	1	0	0	0	0	0	0
13		90	190	750	120	30	603	900	2	1	0	1	1	0	0	0	0	0	0
14	[31]	90	90	1000	150	30	86	500	1	1	0	0	1	0	0	0	0	0	0
15	[32]	0	175	750	100	30	27	20	0	0	0	0	0	1	0	0	0	0	0
16		0	175	550	100	50	27	20	0	0	0	0	0	1	0	0	0	0	0
17		45	175	750	100	30	27	20	0	0	0	0	0	1	0	0	0	0	0
18		45	175	550	100	50	27	20	0	0	0	0	0	1	0	0	0	0	0
19		90	175	750	100	30	27	20	0	0	0	0	0	1	0	0	0	0	0
20		90	175	550	100	50	27	20	0	0	0	0	0	1	0	0	0	0	0
21	[33]	90	200	1000	110	50	661	1038	1	1	0	0	0	0	0	0	0	0	0
22		90	200	1000	110	50	172	1038	1	1	0	0	0	0	0	0	0	0	0
23		90	195	1083	90	20	661	1038	1	1	0	0	0	0	0	0	0	0	0
24		90	195	1083	90	20	172	1038	1	1	0	0	0	0	0	0	0	0	0
25		90	200	1000	110	50	661	1038	1	1	0	1	1	0	0	0	0	0	0
26		90	200	1000	110	50	172	1038	1	1	0	1	1	0	0	0	0	0	0
27		90	195	1083	90	20	172	1038	1	1	0	1	1	0	0	0	0	0	0
28	[34]	0	195	1083	90	20	273	20	0	0	0	1	1	0	0	0	0	0	0
29	[35]	90	275	700	100	50	1005	620	1.5	1	0	0	0	0	0	0	0	0	0
30		90	275	700	100	50	1005	620	1.5	1	0	0	1	0	0	0	0	0	0
31		90	275	700	100	50	60	620	1.5	1	0	0	0	0	0	0	0	0	0
32		90	275	700	100	50	60	620	1.5	1	0	0	1	0	0	0	0	0	0
33		90	275	700	100	50	60	620	1.5	1	0	0	1	0	0	0	0	0	0
34	[36]	90	245	960	100	30	346	900	2	0	1	0	1	0	0	0	0	0	0
35		90	245	960	100	30	346	20	0	0	0	0	1	0	0	0	0	0	0
36	[37]	0	250	1083	90	20	45	20	0	0	0	0	0	0	0	0	0	0	0
37		90	250	1083	90	20	45	20	0	0	0	0	0	0	0	0	0	0	0
38		0	250	1083	90	40	45	20	0	0	0	0	0	0	0	0	0	0	0
39		90	250	1083	90	40	45	20	0	0	0	0	0	0	0	0	0	0	0
40	[38]	0	195	1083	90	20	144	20	0	0	0	0	0	1	0	0	0	0	0
41		0	195	1083	90	20	144	20	0	0	0	0	0	1	0	0	0	0	0
42	[39]	90	195	1083	90	20	294	20	0	0	0	1	1	0	0	0	0	0	0
43		90	195	1083	90	20	294	900	0.2	1	0	1	1	0	0	0	0	0	0
44		90	195	1083	90	20	294	1050	0.2	1	0	1	1	0	0	0	0	0	0
45	[40]	0	180	1200	60	30	161	650	2	1	0	1	0	0	0	0	0	0	0
46	[41]	90	320	2400	100	50	190	20	0	0	0	0	0	0	0	0	0	0	0
47	[42]	90	275	760	120	50	171	20	0	0	0	0	0	0	0	0	0	0	0
48		90	275	760	120	50	171	20	0	0	0	0	0	0	0	0	1	0	0
49		90	275	760	120	50	171	20	0	0	0	1	0	0	0	0	0	0	0
50	[43]	90	113	600	80	20	933	20	0	0	0	1	0	0	0	0	0	0	0

directly from the production settings and with the training process carried out by considering available literature datasets. To achieve the same result with traditional methods, a costly and time-consuming DOE (Design of Experiments), for example, would have been required. Moreover, DOE is not applicable using literature data, as ML. This is the most significant advantage of the proposed ML algorithms over traditional methods. Furthermore, with the developed approach, the variability associated with the ML predictions, dependent on the data available for the training, can be also considered, thus allowing for a safe fatigue design.

3. Machine learning models

This section outlines the probabilistic ML algorithms that have been developed. Details about the FFNN-L and its construction are provided in Section 3.1, whereas in Section 3.2 the PINN-L is defined so that all the training data can be leveraged properly. Lastly Section 3.3 outlines the functioning of the R90C90 BNN and its application to predict the R90C90 Owen's curve.

3.1. FFNN-L

The first model to be introduced is a FFNN trained to predict the parameters of the linear fatigue model. The model, named FFNN-L, predicts the slope m, the intercept q and the standard deviation σ of the linear fatigue model for any given manufacturing configuration. Therefore, the model is trained on 51 data points, each representing a dataset of the TDB (Table 1). An FFNN is a basic type of NN where data flows only in one direction, from the input layer through hidden layers to the output layer. Within the hidden layers, neurons process the features x_j, applying weights w_{ij} and biases b_i to generate a combined signal transformed by an activation function. The output layer typically uses a linear activation which can be a sigmoid, a linear, a rectified linear unit (ReLU), or hyperbolic tangent (tanh) function. Two critical hyperparameters in this process are the number of training iterations (epochs) and the learning rate. During training, the process is repeated for each epoch, and the weights w_{ij} and biases b_i are adjusted after each cycle to enhance prediction accuracy. This adjustment is guided by a loss function, typically mean squared error (MSE) which measures how well the network predictions $y_{i,pred}$ match the desired output $y_{i,true}$. The learning rate determines the update magnitude for weights and biases, balancing between rapid convergence and stability. Another hyperparameter of importance is the batch size, representing the number of data samples processed simultaneously, with mini-batch gradient descent often being a practical choice. For a detailed explanation of FFNN, the reader is referred to [9].

Fig. 1 shows the structure of the first NN employed in this research, the FFNN-L.

As shown in Fig. 1, there are 4 inputs categories, namely PP, V_{risk}, TT and ST. Concerning the PP category, ϑ, P, v, h and t, previously defined, are present. For TT, the numeric variables are T and Δt, whereas *TT_Ann* and *TT_HIP* are booleans. The ST category includes *ST_Mac*, *ST_Pol*, *ST_EP*, *ST_Grind*, *ST_SSP*, *ST_VF*, *ST_Nitr,* and *ST_DN*. These 18 variables are the features, whereas the three labels are m, q and σ. The loss function for this NN is the MSE. The three intermediate hidden layers are characterized by 100, 75 and 50 neurons, respectively, all activated with the ReLU function. Indeed in [9] and in [11,12] it has been shown that a pyramidal structure, further increases the quality of the fatigue performance predictions of PBF-LB parts.

Before each training, the TDB is randomly split into 90 % training and 10 % testing part, yielding 46 training and 5 testing datasets, respectively. Data are normalized following the z-score for each feature ($x_{norm} = (x - x_{train,\mu}) / x_{train,\sigma}$), with the mean and standard deviation of computed on the training dataset. The NN is trained for 1000 epochs with a learning rate equal to 0.001 and the batch size to 30.

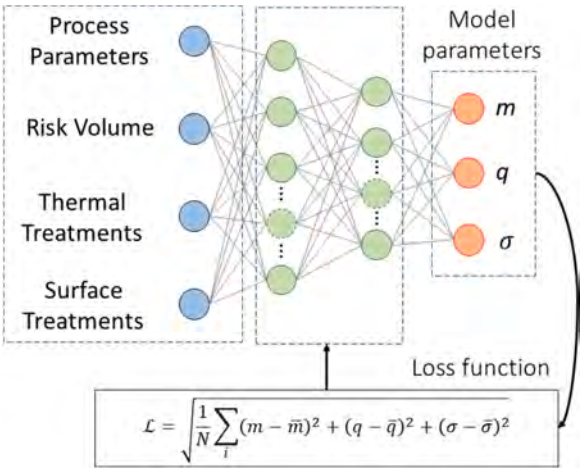

Fig. 1. FFNN-L structure.

3.2. PINN-L

In the FFNN-L, the dataset standard deviation σ is part of the TDB labels, therefore its value should be computed beforehand. As a consequence, since the number of datasets in the TDB is 51, the number of training points is reduced to 51 as well. To overcome this issue and leverage all the 518 training data points, a probabilistic loss function $\mathscr{L}$ (Eq. (4)) is proposed to find the standard deviation associated with each manufacturing configuration by maximizing the log-likelihood of each batch:

$$L = -\sum_{i}^{M}(1 - R_{f,i})\ln\left(PDF\left(log_{10}N_{f,i};\sigma\right)\right) + R_{f,i}\ln\left(1 - CDF\left(\log_{10}N_{f,i};\sigma\right)\right), \tag{4}$$

As for the FFNN-L, the linear fatigue model is assumed, and its parameters are the outputs of the network. Therefore, the proposed PINN outputs m, q, and σ to compute the PDF using Eq. (1). The model can be trained on the full TDB (518 points), provided that an adequate training and testing split is adopted (90 % − 10 % split). This favors model generalization and reduces overfitting. The task is accomplished through a custom loss function that embeds previous physical knowledge into the ML algorithm [45]. Unlike in [11], where the custom loss function calculated the derivative on the SN diagram to force monotonically decreasing behaviors without accounting for the presence of runouts and their statistical significance, here the linear trend is enforced. To obtain this, the PINN structure shown in Fig. 2 is exploited. The same inputs of the NN of Section 2.2 are used, except that S_a and R_f are also included to exploit the full TDB. They are referred to as mock inputs since they are not fed to the NN hidden structure directly, but they are only passed to the custom loss function.

The hidden structure is the same of the previous section, but the number of epochs employed are 5000, the batch size is 300 whereas the learning rate has been set to 0.0001. The number of trainable parameters for this PINN model is the same as the previous FFNN-L, since the fully connected structure remains the same, despite the concatenated mock inputs. For this NN, the testing procedure is more flexible with respect to the previous FFNN. Indeed, the testing part can be composed of randomly selected points, belonging to more datasets (the case in which all points belonging to the same dataset are all removed, is highly unlikely). Otherwise, a dataset testing strategy can be adopted, by removing all the points pertaining to the same dataset, on randomly selected datasets. The latter strategy is more severe [11], but allows to compare the performance of this PINN model to the one of the FFNN of Section 2.2.

3.3. R90C90 BNN

The proposed NN models the aleatoric response of fatigue by embedding the prediction of statistically distributed values of the fatigue life. However, the predicted distributions are inferred from the available data, which in turn affects the predicted response. In principle, the aleatoric distribution should be insensitive to the observed values, but in reality, this can be only achieved if infinite samples are available. To discern the effect of the training data (i.e., the uncertainty of the model) from the intrinsic scattering of the fatigue response (i.e., the aleatoric uncertainty), a BNN is adopted.

BNN allows to capture the ML model uncertainty with ease, granting also the model generalization by considering Bayesian statistics as part of the model. Indeed, in a BNN each weight and bias of a layer is a random variable instead of a single value, whose distributions are defined by maximizing the log-likelihood of the posterior distribution on the observed data. BNN are commonly built with variational layers, using parametric functions (e.g., Bernoulli, Gaussian, Weibull…) for both the prior and posterior distributions. Each layer is defined by the number of neurons, the activation function, the prior distribution, and the posterior distribution. Variational layers are trained by minimizing the Kullback-Leibler (KL) divergence [46,47], which requires the definition of KL weights to preserve consistency. For this BNN, both the prior and posterior are defined as a multivariate normal distributions, that are used to

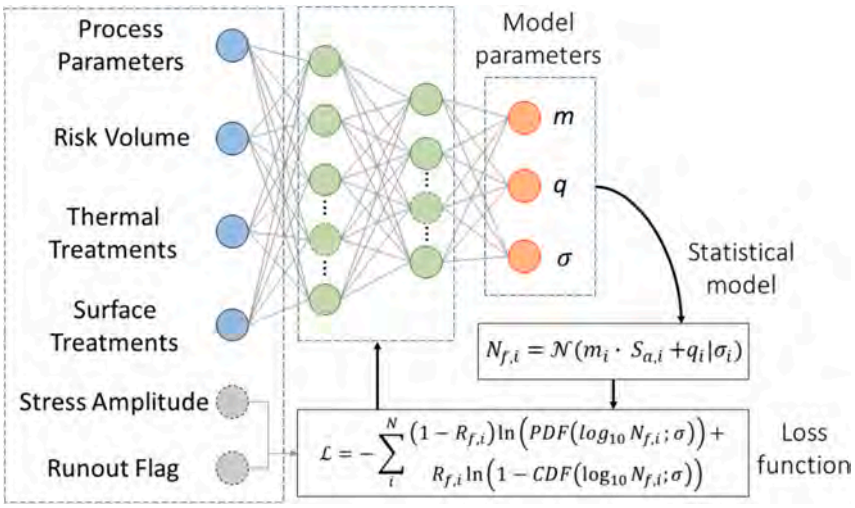

Fig. 2. PINN-L structure. The following NN allows to produce the MLLE fit parameters, but by using all the TDB data.

introduce those uncertainties in the layer connections. The prior is a standardized multivariate normal distribution (zero mean vector and identity covariance matrix) whereas the posterior is a fully populated multivariate normal distribution, whose mean vector and symmetric covariance matrix entries are updated during training. BNN architecture is analogue to the one of FFNN, with the only difference that at least one of the layers is a variational one, whereas for the FFNN-L all layers are deterministic.

Here the goal is to predict N_f at 90 % Reliability (R90) and 90 % Confidence (C90), as defined in Section 2.3, to confine the intrinsic scatter of the fatigue (R90) and the uncertainty of linear model (C90) to the dataset, while modelling the ML uncertainty with the BNN. This allows to assess design PSN curves that can be used to predict fatigue life accounting for the limitations of the ML model related to the available data.

The inputs of the BNN are the PP, V_{risk}, TT, ST and S_a as well. The BNN architecture is reported in Fig. 3. The input layer has 19 nodes, while the 3 deterministic hidden layers have 100, 75 and 50 neurons, respectively, all activated with a ReLU function.

Another single input node is concatenated to the third layer that takes once more S_a as input. The third layer with $50 + 1$ neurons is connected to the variational output layer, which is linearly activated with just 1 neuron. This is done to obtain a mean behavior between the linear and the ReLU activation function to S_a, since the output layer is linearly activated, and the 3rd layer has the ReLU influence of S_a coming from the 19 nodes input layer that has undergone ReLU activations for three times. Therefore, linear behaviors can be obtained (thanks to the linearly activated part of S_a), while having flexible adapting slopes (thanks to the ReLU activated part of S_a).

Nonetheless, the employment of a BNN can favor a better training and model generalization [47], as it will be discussed in the next sections. For the training of the BNN, the batch size has been set to 30, the learning rate to 0.001 and the number of epochs to 1500.

To provide design SN curves that are characterized also by the model uncertainty, the BNN is trained with the N_f defined with R90C90 Owen procedure (Eq. (3)) [22]. In this way, the aleatoric and epistemic uncertainty intrinsic to fatigue experimental campaigns can be separated from the ML model uncertainty.

4. Results and discussion

The proposed models aim at predicting the PSN curves, which account for the probabilistic nature of the fatigue response, and the uncertainty of the fatigue models, properly discerning one from the other. First, the overall accuracy of the models is verified and the predicted PSN curves are compared with the experimental data. Thereafter, the algorithms are further stressed by considering the manufacturing conditions not included in the training database.

The NNs have been developed in Python using the libraries “Tensor Flow” and “Tensor Flow Probability”. The model generalization has been verified by monitoring the loss values computed on the training and test datasets at each epoch. Indeed, if the testing loss diverges above the training loss, it is a clear sign of overfitting [48]. Overfitting is critical in neural networks, especially when a small TDB is used, as in the case of FFNN-L. Fig. 4a shows that the test loss diverges from the training one after 50 epochs [49]. However, such a low number of training epochs would not guarantee sufficient accuracy compared to other models. The tendency of these NN to overfit can be justified by the reduced amount of data, making it less accurate than some other models evaluated in this study. Despite this, the results provide valuable insights for improving model performance.

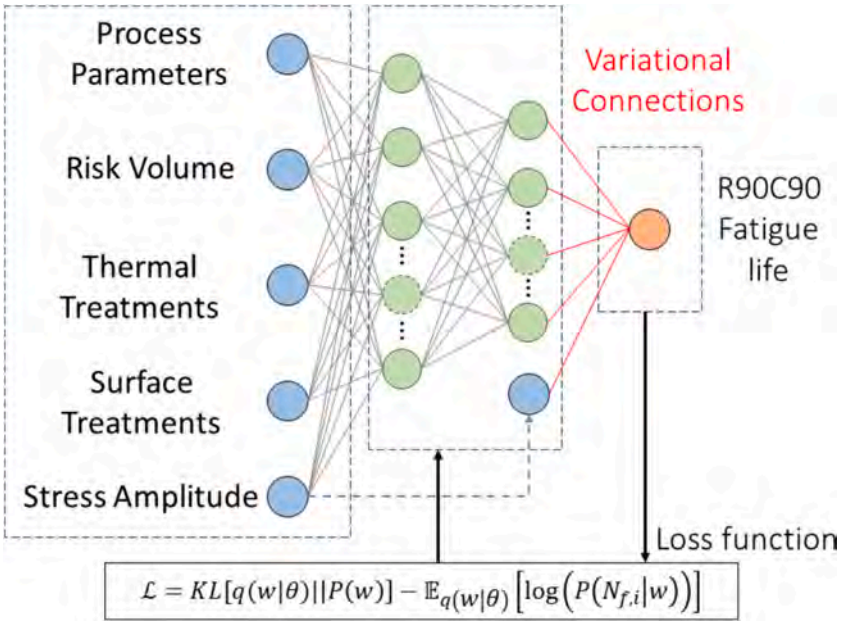

Fig. 3. R90C90 fit BNN structure.

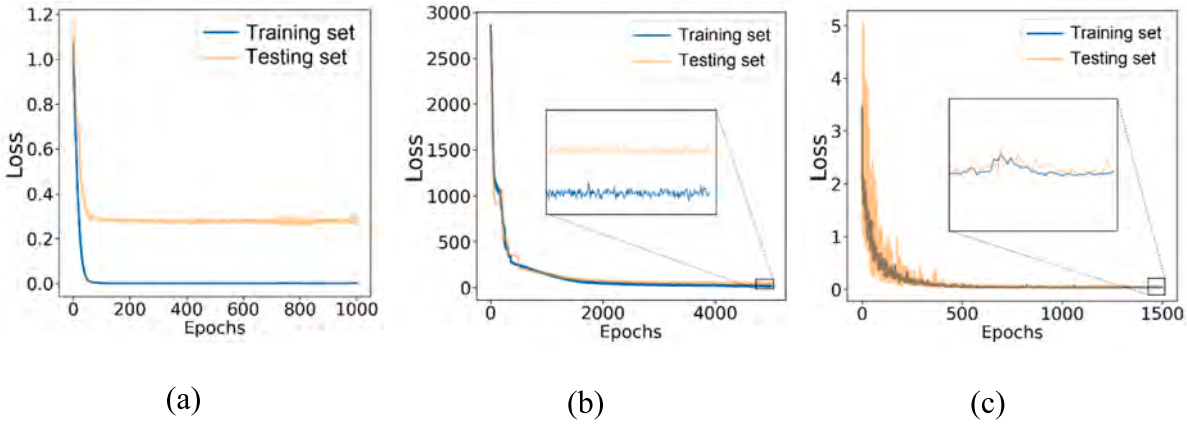

Fig. 4. Training and Testing Losses for the FFNN-L (a), the PINN-L (b) and the R90C90 BNN (c). It can be observed a progressive reduction in the overfitting behavior, from the first NN model to the last one.

The PINN-L training and testing losses follow a similar trend (Fig. 4b), meaning that there is no overfitting or underfitting. Due to its complexity, this model requires more epochs to be trained, eventually achieving subtle differences in the training and testing losses.

Introducing the statistical distributions in the R90C90 BNN connections allows to better generalize and represent the data. In fact, as can be seen from Fig. 4c, the testing loss has a great overlap with the training loss and both curves have a steep training descent. To search for hidden instabilities in the training process, the procedure has been carried until 1500 epochs. As Fig. 4c shows, no problems occurred, meaning that the model is correctly trained and is capable of well generalizing the data.

For normalization, the z-score method was utilized. Regarding feature selection, the approach outlined in [11] was adopted. Due to the limited data availability compared to typical machine learning applications, a single percentage data split of 90 % training and 10 % testing was implemented. In terms of data cleaning, the original dataset consisted of 550 entries, out of which 32 were identified as outliers and removed. For validation, a 90 %-10 % split was selected, aligning with standard practices in the literature.

In Section 4.1 the PSN curves extracted from the FFNN-L are compared with the ones of the PINN-L, and the R90C90 BNN. Section 4.2 explores the influences of the process parameters alone and combined on N_f.

4.1. Probabilistic S-N curves

For the FFNN-L algorithm, all datasets have been evaluated and four of them are shown in this Section (more PSN curves are reported in the Appendix). To maintain an unbiased evaluation, two training sets and two testing sets are randomly drawn. Respectively datasets 0 and 34 (Fig. 5a and c) are coming from training sets while datasets 15 and 48 (Fig. 5b and d) are testing sets (refer to Table 1, for the dataset PP and reference article). For each of the four datasets (from Fig. 5a to Fig. 5d), two figures are shown: the FFNN-L prediction (green) and the PINN-L (red), both compared to the experimental R50 curve (black). Table 2 reports the log-likelihood estimated on the selected datasets, alongside the total value computed over the complete database. Both FFNN-L and PINN-L provide accurate predictions of the PSN curves in the case of training datasets, with an acceptable log-likelihood difference – with respect to the MLLE on the experimental data. However, the PINN-L outperforms the FFNN-L when tested outside the training database (Fig. 5), proving its superior predictive capability. In this case (Fig. 5b and g), the FFNN-L provided a PSN curve with a significantly lower MLLE (1.782 and −60.86) compared to the one obtained fitting the linear model on the experimental data (9.595 and −7.104), while the PINN-L (Fig. 5d and i) correctly estimates the PSN curve, achieving a higher MLLE compared to the FFNN-L (4.057 and −8.215). An overall comparison reported in Table 2 accounts for all the data points, i.e., the total sum of the MLLE, underlining that the PINN-L consistently gives more accurate results.

The lower accuracy of the FFNN-L is imputable to the size of the TDB, which only comprises 51 points, one for each dataset. This gap suggests that, while the FFNN-L fits the training data very well, it does not generalize as well to the test data. It may be concluded that the model is capturing noise and details specific to the training data, which negatively affect the accuracy in the test case.

The modified training strategy employed in the PINN-L allows to use the full TDB, to improve the model generalization.

Fig. 5d and 5 h, show the PSN curves predicted with the PINN-L model on the test datasets. An overall improvement in the model accuracy is observable, as indicated in Table 2, imputable to the increase in the database size. As an example, the training dataset 34 is correctly predicted by the PINN-L, as opposed to the FFNN-L (Fig. 5c).

However, not in all cases the slope is properly estimated (Fig. 5d and h) by the PINN-L. This behavior is particularly evident for datasets with a limited amount of data, where the R90-R10 bands correctly contain the majority of experimental points, but the m and q are not always correctly estimated. Indeed, the model compensates for the small numerosity of training data by increasing the predicted standard deviation σ, compromising the accuracy on the slope and intercept parameters, m and q. The correlation between the predicted deviation and the dataset size is analysed in Fig. 6a and b.

It is possible to appreciate how the PINN-L compensates for the limited numerosity of training data by increasing the associated

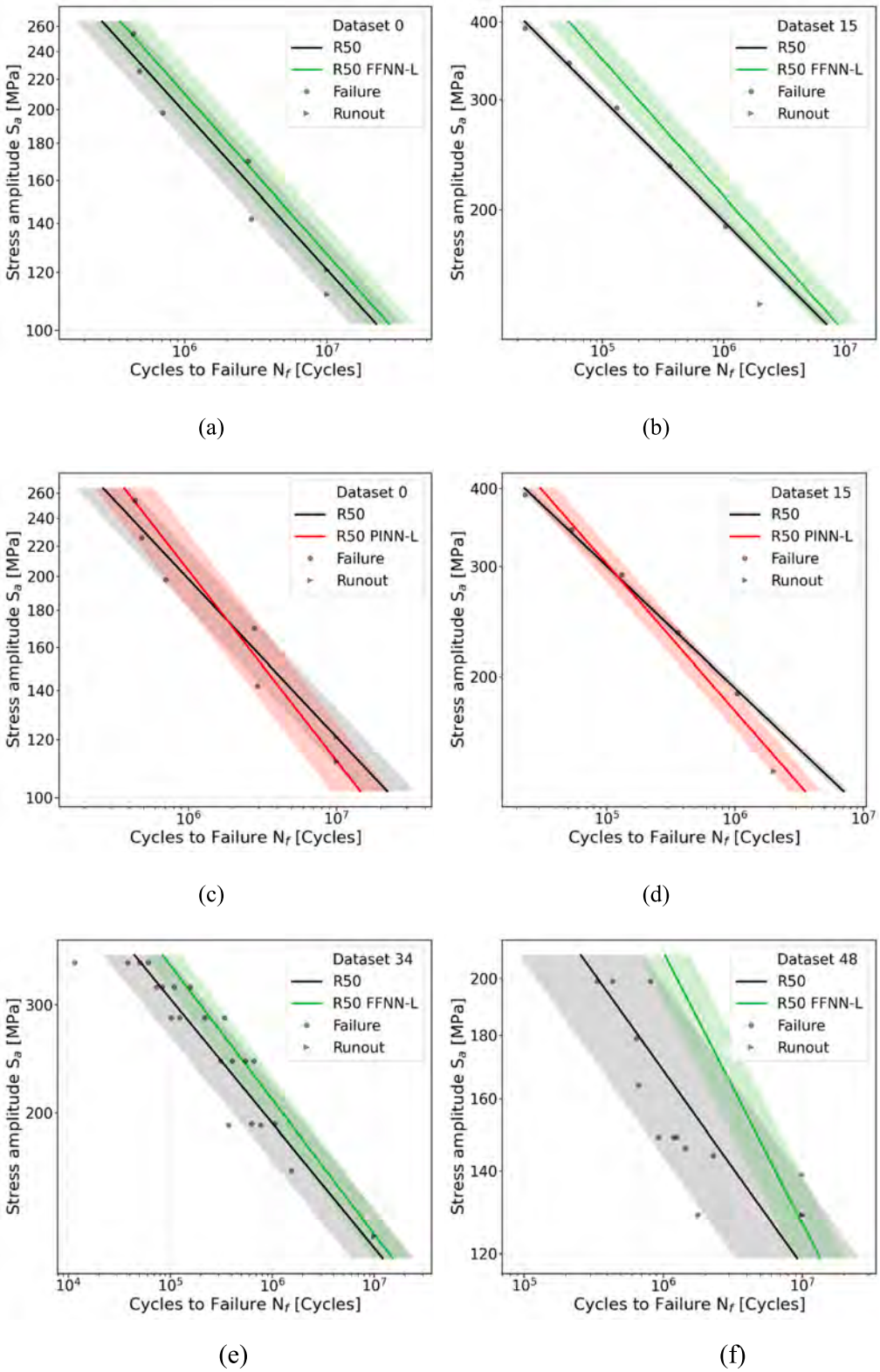

Fig. 5. FFNN-L and PINN-L PSN curves. In black the MLLE experimental fit, while in green the FFNN-L predictions and in red the PINN-L predictions. The green, red and black transparent bands are the R90-R10 bands. (b) and (d) are testing sets, whereas the others are training sets.

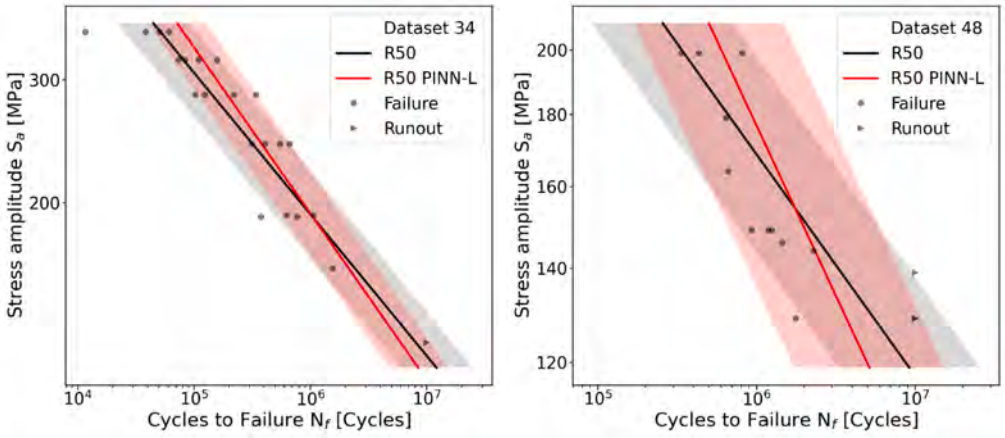

(g) (h)

Fig. 5. (*continued*).

Table 2
Experimental, FFNN-L and PINN-L MLLE for the shown training and testing datasets. The row total accounts for the sum of the MLLE of all 51 datasets. The PINN-L outperforms the FFNN-L since its MLLE is significantly higher.

Dataset	Experimental	FFNN-L	PINN-L	Training	Testing
0	1.658	1.485	0.444	x	
15	9.595	1.782	4.057		x
34	−0.851	−15.804	−5.097	x	
48	−7.104	−60.864	−8.215		x
Total	132.275	−4887.481	−51.226		

uncertainty via the predicted σ. In detail, the PINN-L has been firstly interrogated with fixed features (set to the TDB most recurrent values, as it has been done for Section 4.2), while varying the studied PP, one at a time. The kernel density estimate (blue) has been superimposed to demonstrate that when there is a large amount of data, as in the 150–280 W range for *P* (Fig. 6a) and the 80–110 μm

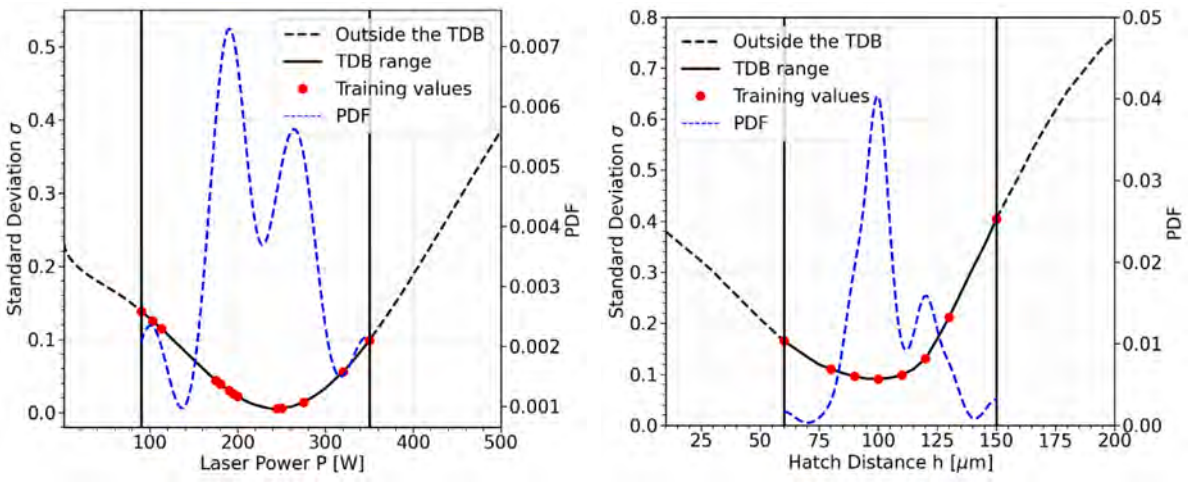

(a) (b)

Fig. 6. Standard deviation σ estimated by the PINN-L as the PP varies (P in a, h in b). The red points correspond to the actual training values in the TDB. The dashed black line refers to the PP range outside the TDB, while its plain counterpart refers to the training range. In dashed blue the kernel density estimate.

range for h (Fig. 6b), the predicted σ is small. On the other hand, where the numerosity of the training data is limited (dashed black line outside the TDB range and in the training range boundaries), the uncertainty associated with the prediction drastically increases.

To separate the experimentally observed uncertainty from the prediction uncertainty, the BNN is introduced. In the BNN, the probabilistic formulation of its parameters can capture the input-related uncertainty and discern it from the experimental scattering. Moreover, the probabilistic formulation of the BNN weights allows to improve the generalization capability of the model [47]. This behavior can be appreciated not only from the training and testing loss curves, but also from the R90C90 curves. Considering Owen's R90C90 curve, with this BNN, allows to model effectively the model uncertainty on these design curves while guaranteeing that the ML model uncertainty is separated from the uncertainty of experimental data. This was not possible with the deterministic formulation of the FFNN-L and with the PINN-L, whose probabilistic approach was not inherited in the weight uncertainty of their NN formulation. Considering these factors, the chosen ML model successfully addresses the challenges of predicting and preventing fatigue failures, ensuring accurate and reliable results. Among these models, neural networks (NNs) stand out as the most suitable technique for describing and addressing the fatigue behavior of additively manufactured (AM) metal alloys, thanks to their exceptional performance

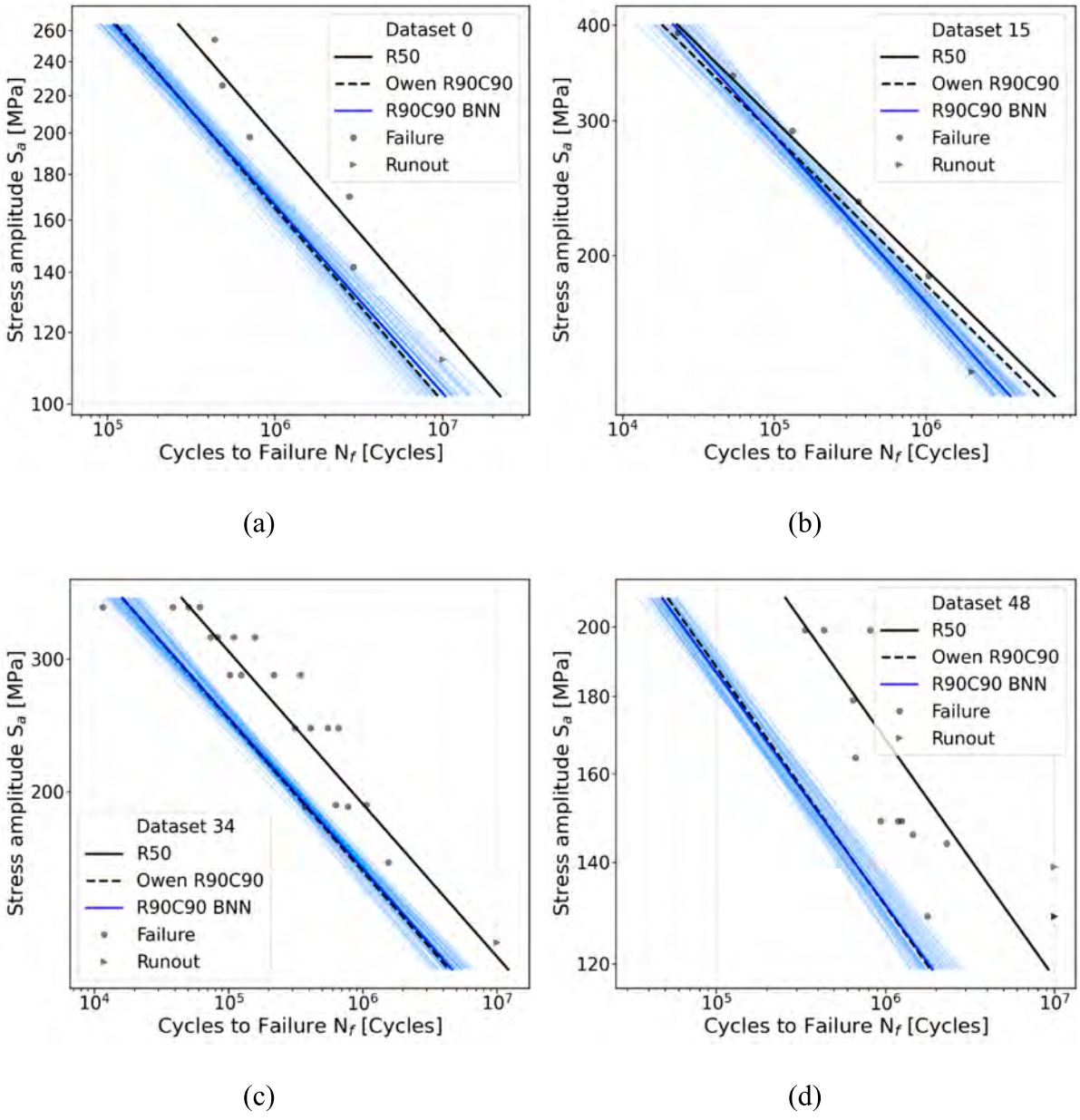

Fig. 7. BNN PSN curves. In black the R50 experimental fit, in dashed black the Owen R90C90 curve, in light blue the R90C90 BNN predictions and in blue their mean. (b) and (d) are testing sets, whereas the other four are training sets.

and flexibility. This conclusion is further supported in [9], where a review of machine learning techniques for predicting the fatigue response of AM parts was conducted. Specifically, the analysis in [9] highlighted that NNs are among the most effective ML algorithms for this particular application. Indeed, from Fig. 7 it is possible to appreciate this behavior. For each dataset, the BNN is interrogated 100 times for each S_a level, and 100 BNN curves (light blue) and their mean (blue) can be computed and plotted on top of the R90C90 experimental curve (dashed black). It is possible to appreciate how the results are greatly improved for the same training (Fig. 7a and c) and testing (Fig. 7b and d) sets, used also for the previous NN. The model predictions can outline which regions of the dataset are less confident and which ones are more certain. It can be understood how the S_a levels around 250 MPa output a tighter prediction band, whereas the upper and lower extrema (namely 400 and 100 MPa) produce a less confident band. This behavior can be mainly ascribed to a higher density of experimental points around 250 MPa and to a lower one around 100 and 400 MPa in the TDB. The BNN automatically accounts for these discrepancies by adjusting the weight uncertainty and increasing the associated standard deviation. Due to these reasons and the ones explained in Section 3.3, this particular model proves to be the most generalizable, reliable and flexible.

It must be noted that, during the fatigue design stage, a unique PSN design curve should be available rather than a band of curves. According to Fig. 8, the 10th curve of the BNN prediction envelope can be considered as the BNN C90 curve and is characterized by an offset with respect to the R90C90 Owen's experimental fit (dashed black) and the BNN mean (blue), indicating how confident the BNN prediction is. This curve, with this R90C90 BNN, is the one to be used to design against fatigue failures for PBF-LB SS316L when considering the influence of PP. This approach has been validated on the PBF-LB SS316L, but it can be generalized and extended to other materials. Fig. 8 shows the advantages of employing a BNN: with this ML model is possible to separate the epistemic uncertainty contribution related to the ML algorithm, from the aleatoric and epistemic uncertainty contributions that are tied to the Owen's R90C90 fatigue design curve.

Table 3. resumes the NN models employed for this research, listing their details, objectives, advantages and disadvantages in a compact manner.

4.2. Process parameters influence

Once the BNN has been correctly trained, it can be used to produce continuous predictions to evaluate the PP influence on the fatigue life. Since S_a ranges from 100 to 400 MPa in the TDB, the 200 and 350 MPa levels have been chosen, i.e., the stress amplitudes where a larger amount of data is available. In this parametric study, specific parameters have been varied while all the remaining input features have been set to their most recurrent values (Table 4).

In Section 4.2.1 the effect of a single parameter is studied, specifically ϑ, P, v, h, and t. Section 4.2.2 evaluates the synergic effect of P and v, h and t, and of E_d and ϑ. In this Section the word "life" is always referred to as the R90C90 N_f predicted by the BNN.

4.2.1. Single parameter influence

Fig. 9a shows the effect of ϑ on the fatigue life. The model is in agreement with the experimental results which demonstrate that horizontally manufactured specimens (0°) have a better fatigue life than the vertically manufactured ones (90°) [2,27,50,51].

In the case of P, v, h, and t, the predictions have been extended outside the respective range observed in the TDB, as indicated by black dashed lines in Fig. 9b and 9e. Therefore, the training ranges, as maximum and minimum values, found in the TDB are

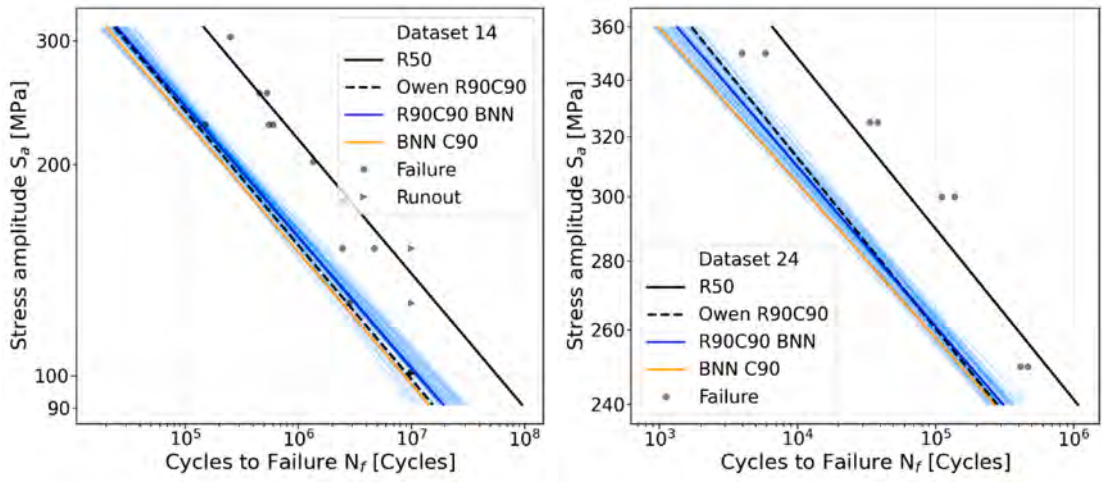

(a) (b)

Fig. 8. PSN curves BNN model uncertainty at a model confidence level of 90% (Orange) for two datasets. Within the uncertainty bands, the 10th element can be selected to provide the C90 BNN R90C90 design curve.

Table 3
NN models comparison.

NN	Details	Objective	Advantages	Disadvantages
FFNN-L	– Dataset TDB (51 data) – 18 inputs – Pyramidal structure of 100, 75 and 50 ReLU neurons – 3 outputs – epochs: 1000 – learning rate: 0.001 – batch size: 30	Predict m, q and σ for each dataset from PP, V_{risk}, TT, ST	– Simple model – Simple loss function – Fast Training – Preliminary employment	– Overfitting – Less training data – Imprecise – Cannot separate experimental uncertainty from model uncertainty
PINN-L	– Full TDB (518 data) – 18 inputs (+2 mock inputs for S_a and R_f) – Pyramidal structure of 100, 75 and 50 ReLU neurons – 3 outputs (+2 mock outputs for S_a and R_f) – epochs: 5000 – learning rate: 0.0001 – batch size: 300	Predict m, q and σ for each dataset from PP, V_{risk}, TT, ST, S_a and R_f using all the data	– Generalization – More training data – More precise than FFNN-L	– Long training – Stiff PSN curve adaptivity – Cannot separate experimental uncertainty from model uncertainty – Complex loss function – Complex model
R90C90 BNN	– Full TDB (518 data) – 19 inputs (S_a concatenated) – Pyramidal structure of 100, 75 and 50 ReLU neurons – 1 variational output – epochs: 1500 – learning rate: 0.001 – batch size: 30	Predict R90C90 N_f from PP, V_{risk}, TT, ST and S_a considering also the model uncertainty	– Generalization – More training data – Fast Training – Can separate experimental uncertainty from model uncertainty – Can directly output the model uncertainty envelope	– Complex model

respectively: from 0° to 90° for ϑ, from 90 W to 350 W for P, from 420 mm/s to 1200 mm/s for v, from 60 μm to 150 μm for h, and from 20 μm to 50 μm for t. Fig. 9b shows that low values of P have a positive effect on the life, particularly below 250 W, while powers above this value lead to a decrease of the fatigue life. Similar trends can be found in [23] for P with respect to the porosity [%], which is associated with a lower life since the defect number and size increase. Also, in [24], it has been shown that increasing P leads to a decrease in ρ_{rel} of PBF-LB SS316L, eventually reflecting in reduced life. In [25], the same trend for P vs ρ_{rel} has been reported, with a drastic decrease of ρ_{rel} after 285 W.

Fig. 9c shows the effect of v on the life. The BNN shows that speeds close to 1200 mm/s give the highest life, especially for the 200 MPa level. The 350 MPa level shows no significant differences between speeds level with the highest life located between the 800 and 1000 mm/s range. However, the 350 MPa is affected by a higher degree of uncertainty, since there are less points in the TDB. As a result, the uncertainty band associated with 350 MPa is larger for all the analyzed PP. Nonetheless, in [52,53], it has been shown that the lowest percentage of porosity is achieved by speeds close to 1250 mm/s, whereas, in [23], similar trends in porosity have been achieved for the 1000 mm/s range. [24] showed that the 800 to 1200 mm/s speed range gives high values of ρ_{rel}, with 1200 mm/s giving the highest ρ_{rel}. Values of v higher than 1200 mm/s led to a drastic decrease of ρ_{rel} and should therefore be avoided. In [25] again, 1200 mm/s leads to the highest ρ_{rel}. The results obtained for v are sound with the experimental evidence, proving the effectiveness of the BNN in modelling the life as the PP changes.

Fig. 9d shows that with small values of h a better fatigue response can be achieved. This behavior is particularly evident for the 350 MPa stress level. At 200 MPa there is no marked difference between values of h ranging from 60 to 90 μm, whereas a more prominent decrease is observed after this range. Once again, the BNN shows an increase in the uncertainty level for the 350 MPa level and if the life is evaluated for h values that are outside of the training range. This BNN behavior is also confirmed by the experimental evidence [54]: as in [23], low values of h lead to low levels of porosity while high values give the opposite behavior. In [25], the authors confirm that low values of h give a higher ρ_{rel}, and vice versa.

In Fig. 9e, it can be observed how t has a more marked influence on the life for the 200 MPa level with respect to the 350 MPa level, but it can be observed that low values of t generally give a better fatigue response. It is generally known that t has a lower influence on the life [11,12,17,18] and Section 4.2.2 analyzes this peculiarity. Nonetheless, [23] confirms the trends found by the BNN, since low values of t produce a lower porosity in the specimens, and in [24] small t led to a higher ρ_{rel}.

It must be remarked that the results shown in Fig. 9 may change if the PP that have been kept constant are altered from the configuration shown in Table 4.

Table 4
TDB Most recurrent values used for the PP effect evaluation. The studied parameter is varied while the others are kept constant.

ϑ [°]	P [W]	v [mm/s]	h [μm]	t [μm]	V_{risk} [mm^3]	T [°C]	Δt [hours]	TT_Ann	TT_HIP	ST_Mac	ST_Pol	ST_EP	ST_Grind	ST_SSP	ST_VF	ST_Nitr	ST_DN
90	275	1000	100	30	600	20	0	0	0	0	0	0	0	0	0	0	0

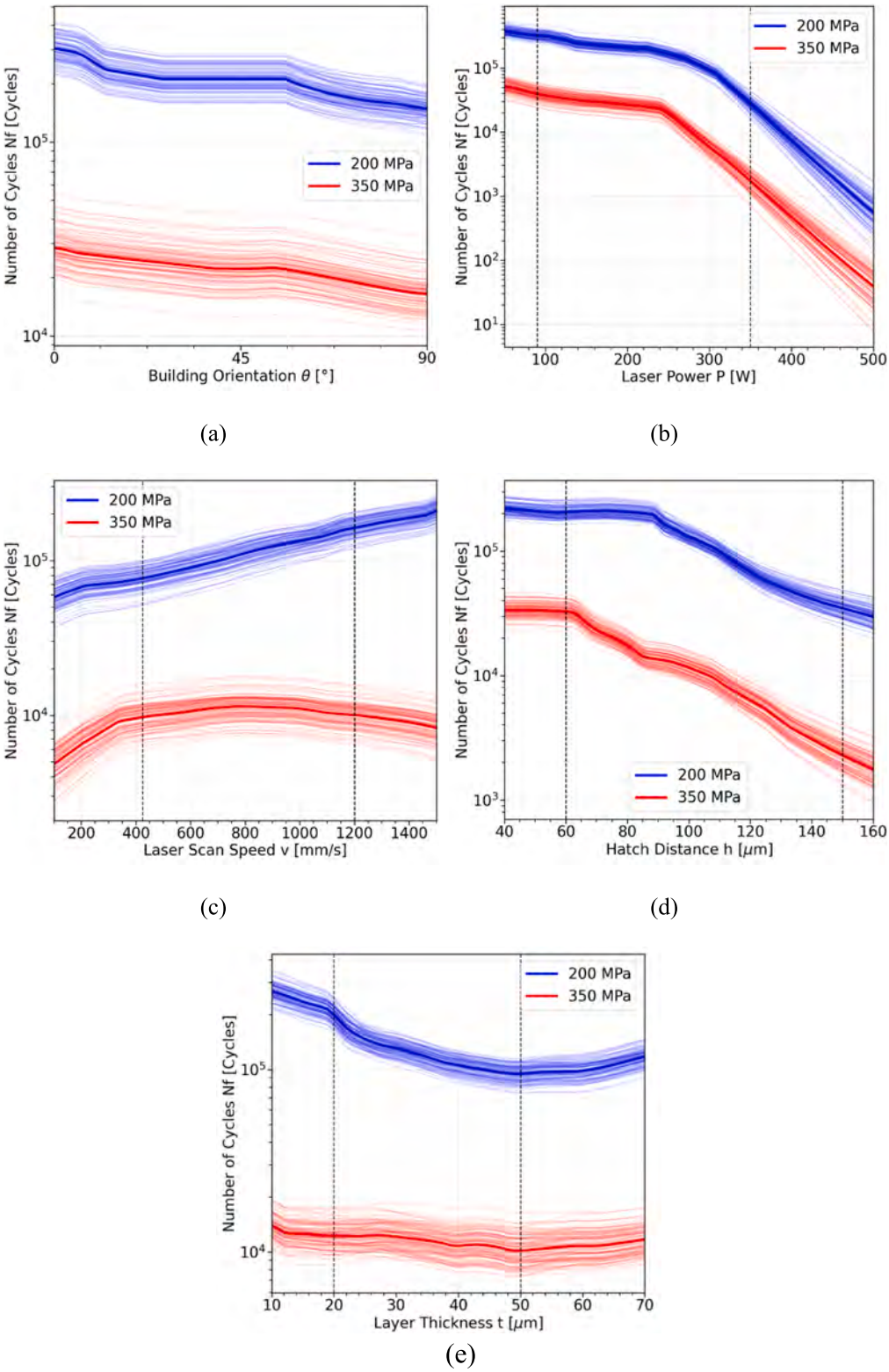

Fig. 9. Effects of ϑ (a), P (b), v (c), h (d) and t (e) on the R90C90 fatigue life N_f, evaluated by the R90C90 BNN, for two different S_a level.

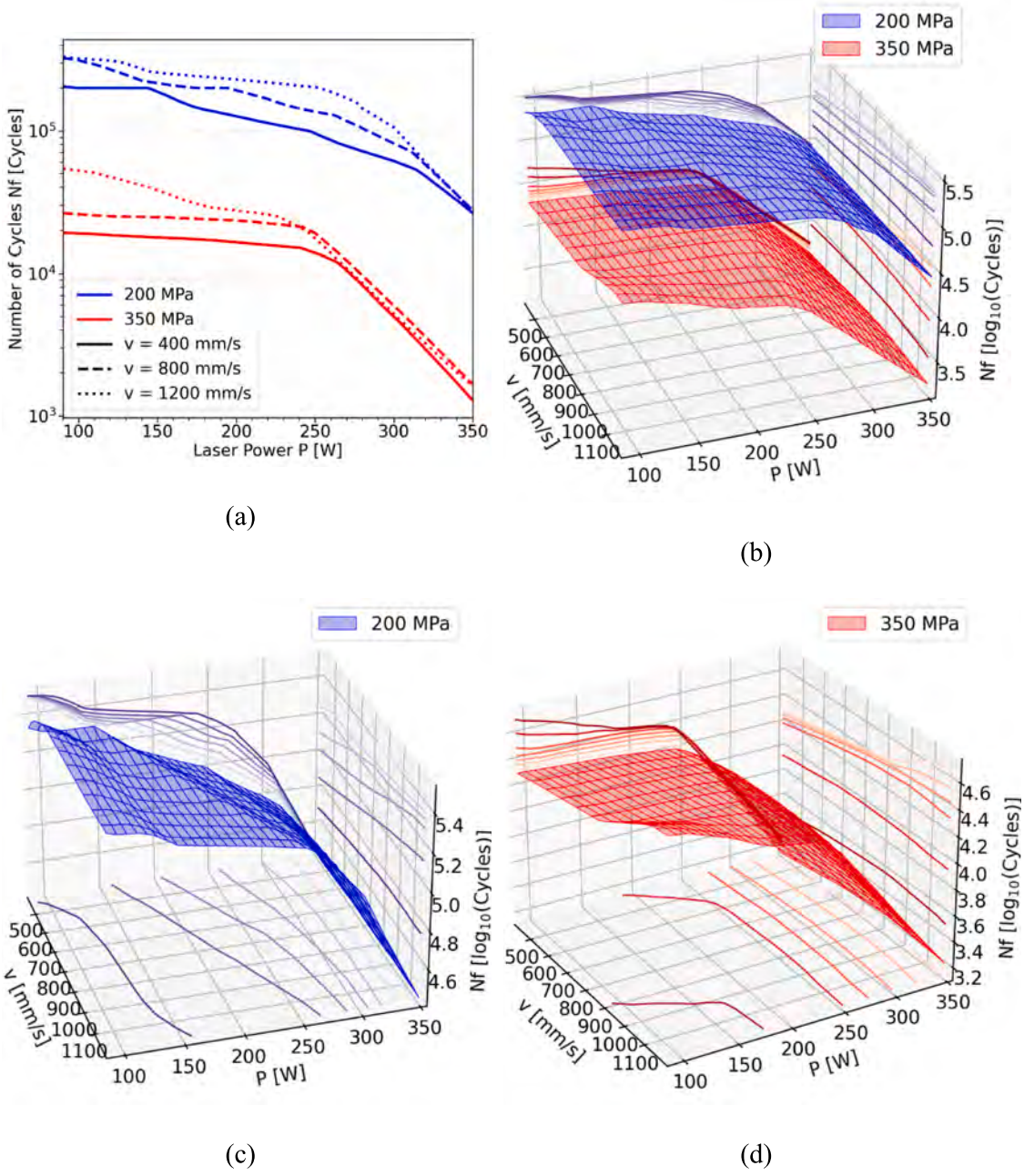

Fig. 10. P and v synergic influence on the R90C90 Nf. In (a) P vs N_f at two Sa levels and at three v levels. In (b) 3d plot of P and v vs R90C90 N_f at 350 and 200 MPa, together (b) and alone with beach contour lines (c and d).

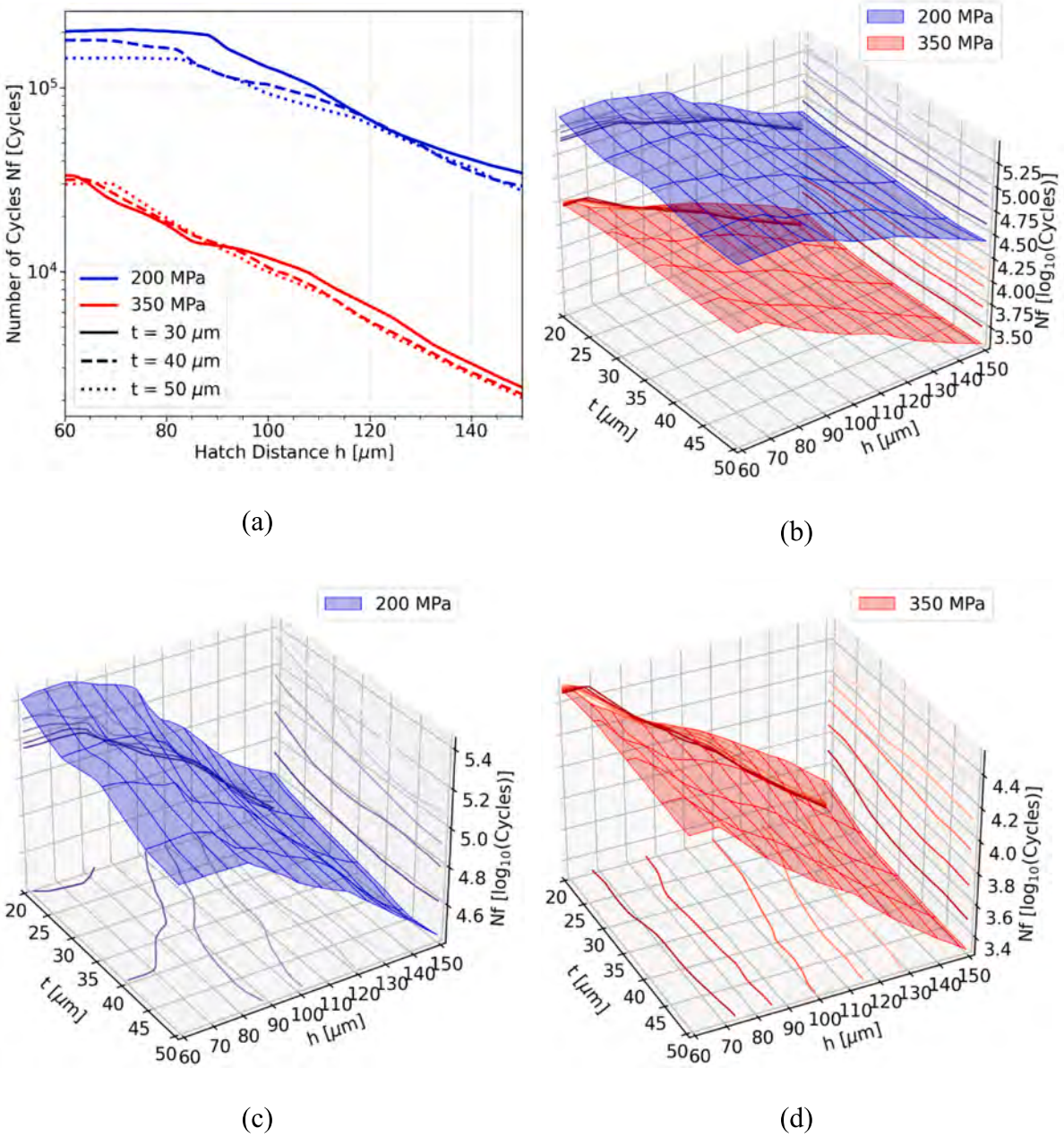

Fig. 11. H and t synergic influence on r90c90 n_f. In (a) h vs N_f at two S_a level and at three t levels. In (b) 3d plot of h and t vs R90C90 N_f at 350 and 200 MPa, together (b) and alone with beach contour lines (c and d).

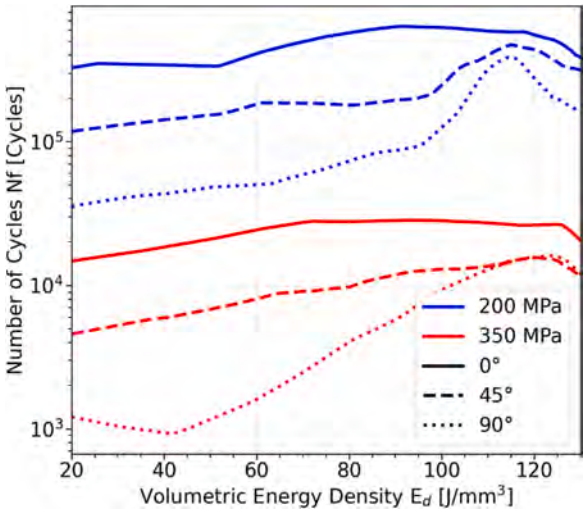

Fig. 12. Effect of E_d on the R90C90 N_f for the three building orientations.

4.2.2. Parameters synergic influence

Experimental results have shown that the correlation between process parameters plays a significant role in the resultant porosity, which in turn affects the fatigue life. In the following, the synergic influence of the PP is analyzed with the BNN. Fig. 10 shows the mutual influence of P and v on the life inside the training range, under different perspectives. It can be observed that P influences the life much more than v. Fig. 10c-d indicates that the highest life is achievable by using high speed combined with a power below 250 W. The influence of v is more marked for low P values, whereas it tends to reduce significantly for high P values (Fig. 10a), suggesting a predominant effect of the excessive power in reducing the fatigue performance. Moreover, the contour lines in Fig. 10c-d highlight the different effects of the parameters interaction at a stress amplitude of 200 MPa and 300 MPa, respectively. Similar trends are found in [25] for ρ_{rel} as opposed to N_f, further proving the excellent capabilities of the BNN.

The combined influence of h and t is reported in Fig. 11. It is evident how t has a limited influence on the fatigue life, while h has a remarkable effect. This is also clear from Fig. 11a where the *iso-t* lines are almost superimposing. However, it can be observed that decreasing t leads to a slightly better response. To achieve a higher fatigue performance, both t and h should be set to their lowest values. However, this could significantly impact the duration of the manufacturing process.

The effect of all the PP combined can be investigated by studying how the volumetric energy density E_d [J/mm^3] affects the response as ϑ varies. Indeed, it is known [23] that E_d is calculated according to Eq. (5), which shows how P, v, h and t are all taken into account at once. The range of evaluation of E_d spans from the minimum to the maximum of the TDB. E_d is calculated for each dataset as:

$$E_d = \frac{P}{v \bullet h \bullet t} \tag{5}$$

Fig. 12 confirms that the 0° configuration outperforms the 45° and this last one on the 90°. The differences between ϑ are less evident in the higher end of E_d, especially for the 350 MPa level. When it comes to E_d, a higher response is achieved for both S_a levels in the range close to 100 and 120 J/mm^3, for the 45° and 90° specimens. A wider plateau of peak response is observable for the horizontal specimens (0°) from 70 ÷ 80 to 120 J/mm^3. The results for E_d obtained with the BNN are also confirmed by the literature. In [52,54], it has been shown that when $E_d = 117$ J/mm^3 a lower number of defects with a smaller size is obtained, leading to a better fatigue life. On the other hand, approaching values of E_d close to 50 J/mm^3 leads to a nonnegligible decrease of the fatigue response, while increasing it too much (close to 300 J/mm^3) drastically increases the size and number of defects leading to an extremely poor fatigue life. In [23], E_d has been set from 20 to 85 J/mm^3, and the measured porosity has trends similar to the trends of the life predicted by the BNN of Fig. 12, since the minimum is achieved on the higher end of the range. Even though E_d is known not to be an exhaustive predictor of fatigue behaviour [54], its influence on the fatigue life has been studied for the sake of comparison with literature results. Indeed, the proposed BNN can provide uncertainty envelopes for any synergic parameter, while preserving the multiple parameters interactions which govern the fatigue strength. However, since more than one PP is considered at once, it has been decided to keep the figures as clear as possible for this chapter.

5. Conclusions

This work presents a novel approach to reliably predict and prevent fatigue failures in additively manufactured (AM) SS316L components. The method is a substantial shift from the use of deterministic machine learning (ML) models to estimate the SN curves, towards probabilistic ones to provide Probabilistic Stress-Life (PSN) curves. Furthermore, the method builds upon established fatigue models, offering a more robust and trustworthy way to adopt ML in fatigue design, leveraging on experimental data. In particular:

- A standard Feed Forward Neural Network (FFNN) is trained to predict the parameters of linear PSN curves from the manufacturing parameters, showing promising results but limited predictive capabilities outside the training intervals
- A variation of the FFNN with a custom loss function is developed to improve the training process, leading to substantial improvements of the model accuracy in extrapolating outside the training database. However, the statistical deviation is concurrently influenced by the experimental scatter and the available data.
- A Bayesian neural network (BNN) is proposed to specifically estimate the uncertainty of the ML model, uniquely related to its architecture and training. To separate this uncertainty from the experimental scattering, the BNN is trained on PSN curves at 90 % reliability (R90) and confidence (C90) levels, commonly used for the industrial practice.
- The results of the BNN are R90C90 curves with a distribution directly inherited from the training dataset, which gives an indication of the trustworthiness of the ML predictions and provides a safe data-driven tool for the design of AM parts.
- All the ML models are trained on literature data that study the critical role of process parameters, risk volume, thermal treatments, and surface treatments in determining fatigue performance. The models allow to assimilate the different scientific findings and embed them into a unique powerful design tool.
- The influence of building orientation, laser power, scan speed, hatch distance, and layer thickness are analysed with the BNN, unveiling their individual and combined effects on fatigue performances. Alongside average trends, the BNN estimates the confidence of the ML prediction outside the training range. The confidence bands could be used to selectively enlarge the database with experiments specifically designed to reduce the model uncertainty under specific manufacturing configurations yet unexplored.

In conclusion, the proposed BNN substantially improves the trustworthiness and explainability of ML models for the fatigue design, providing powerful data-driven tools that accurately predict PSN curves from process parameters, while embedding a probabilistic metric of the ML confidence that can be used to deliver safe design. Its integration into the AM design process offers a significant advancement in producing safer and more reliable components for the aerospace, medical, and automotive industries, as the predicted PSN curve can be chosen with designer-defined confidence level.

Funding

This research did not receive any specific grant from funding agencies in the public, commercial, or not-for-profit sectors.

CRediT authorship contribution statement

Alessio Centola: Writing – original draft, Visualization, Validation, Software, Methodology, Investigation, Data curation, Conceptualization. **Alberto Ciampaglia:** Writing – review & editing, Validation, Supervision, Conceptualization. **Davide Salvatore Paolino:** Writing – review & editing, Supervision, Project administration, Conceptualization. **Andrea Tridello:** Writing – review & editing, Supervision, Project administration, Formal analysis.

Declaration of competing interest

The authors declare that they have no known competing financial interests or personal relationships that could have appeared to influence the work reported in this paper.

Appendix:. Additional results

In the following section, additional PSN curves are shown for two training datasets, namely 9 (Fig. 13a) and 35 (Fig. 13b), evaluated with the FFNN-L, PINN-L and R90C90 BNN.

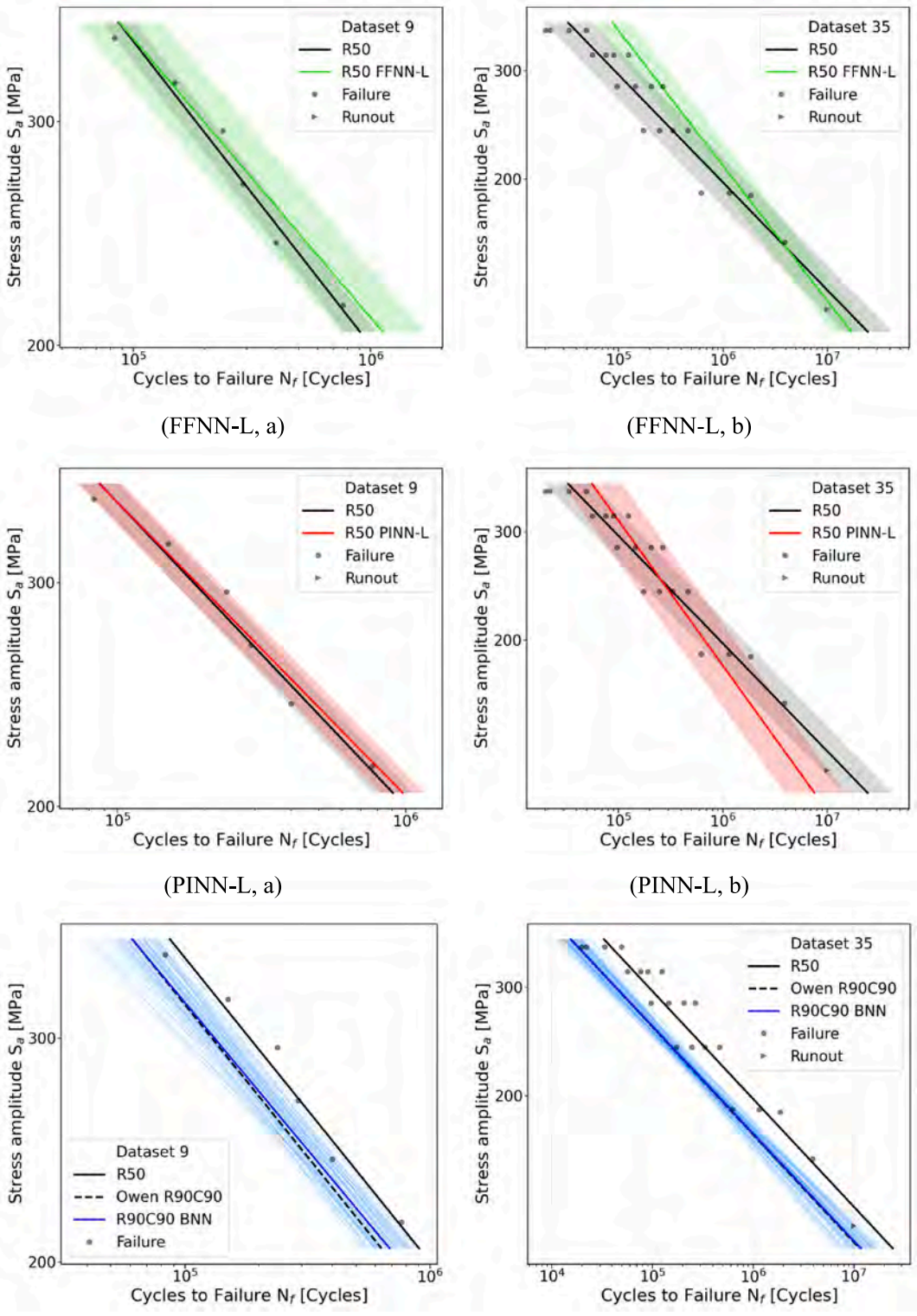

Fig. 13. Additional PSN curves for two training datasets, namely 9 (a) and 35 (b). The green curves have been evaluated with the FFNN-L, the red ones with the PINN-L and the blue ones with the R90C90 BNN.

.

Data availability

Data will be made available on request.

References

[1] Y. Yamashita, T. Murakami, R. Mihara, M. Okada, Y. Murakami, Defect analysis and fatigue design basis for Ni-based superalloy 718 manufactured by additive manufacturing, Procedia Struct. Integrity (2017), https://doi.org/10.1016/j.prostr.2017.11.054.

[2] A. Tridello, J. Fiocchi, C.A. Biffi, G. Chiandussi, M. Rossetto, A. Tuissi, D.S. Paolino, Effect of microstructure, residual stresses and building orientation on the fatigue response up to 109 cycles of an SLM AlSi10Mg alloy, Int. J. Fatigue 137 (2020) 105659, https://doi.org/10.1016/J.IJFATIGUE.2020.105659.

[3] J. Eckert, J.C. Holzer, C.E. Krill, W.L. Johnson, Structural and thermodynamic properties of nanocrystalline fcc metals prepared by mechanical attrition, J. Mater. Res. 7 (1992), https://doi.org/10.1557/JMR.1992.1751.

[4] S. Liu, Y.C. Shin, Additive manufacturing of Ti6Al4V alloy: a review, Mater. Des. 164 (2019), https://doi.org/10.1016/j.matdes.2018.107552.

[5] A. Tridello, J. Fiocchi, C.A. Biffi, G. Chiandussi, M. Rossetto, A. Tuissi, D.S. Paolino, VHCF response of Gaussian SLM AlSi10Mg specimens: Effect of a stress relief heat treatment, Int. J. Fatigue 124 (2019), https://doi.org/10.1016/j.ijfatigue.2019.02.020.

[6] A. Tridello, J. Fiocchi, C.A. Biffi, M. Rossetto, A. Tuissi, D.S. Paolino, Size-effects affecting the fatigue response up to 109 cycles (VHCF) of SLM AlSi10Mg specimens produced in horizontal and vertical directions, Int. J. Fatigue 160 (2022), https://doi.org/10.1016/j.ijfatigue.2022.106825.

[7] Y. Murakami, Metal fatigue: Effects of small defects and nonmetallic inclusions, 2019. doi: 10.1016/C2016-0-05272-5.

[8] F. Calignano, D. Manfredi, E.P. Ambrosio, L. Iuliano, P. Fino, Influence of process parameters on surface roughness of aluminum parts produced by DMLS, Int. J. Adv. Manuf. Technol. 67 (2013), https://doi.org/10.1007/s00170-012-4688-9.

[9] A. Centola, A. Tridello, A. Ciampaglia, F. Berto, D.S. Paolino, Review on machine learning techniques for the assessment of the fatigue response of additively manufactured metal parts, Fatigue Fract. Eng. Mater. Struct. (2024), https://doi.org/10.1111/ffe.14326.

[10] J. Chen, Y. Liu, Fatigue modeling using neural networks: a comprehensive review, Fatigue Fract. Eng. Mater. Struct. 45 (2022), https://doi.org/10.1111/ffe.13640.

[11] A. Centola, A. Ciampaglia, A. Tridello, D.S. Paolino, Machine learning methods to predict the fatigue life of selectively laser melted Ti6Al4V components, Fatigue Fract. Eng. Mater. Struct. 46 (2023), https://doi.org/10.1111/ffe.14125.

[12] A. Tridello, A. Ciampaglia, F. Berto, D.S. Paolino, Assessment of the critical defect in additive manufacturing components through machine learning algorithms, Appl. Sci. (switzerland) 13 (2023), https://doi.org/10.3390/app13074294.

[13] E. Maleki, S. Bagherifard, M. Guagliano, Correlation of residual stress, hardness and surface roughness with crack initiation and fatigue strength of surface treated additive manufactured AlSi10Mg: Experimental and machine learning approaches, J. Mater. Res. Technol. 24 (2023) 3265–3283, https://doi.org/10.1016/J.JMRT.2023.03.193.

[14] L. Dang, X. He, D. Tang, Y. Li, T. Wang, A fatigue life prediction approach for laser-directed energy deposition titanium alloys by using support vector regression based on pore-induced failures, Int. J. Fatigue 159 (2022), https://doi.org/10.1016/j.ijfatigue.2022.106748.

[15] J. Horňas, J. Běhal, P. Homola, S. Senck, M. Holzleitner, N. Godja, Z. Pásztor, B. Hegedüs, R. Doubrava, R. Růžek, L. Petrusová, Modelling fatigue life prediction of additively manufactured Ti-6Al-4V samples using machine learning approach, Int. J. Fatigue 169 (2023) 107483, https://doi.org/10.1016/J.IJFATIGUE.2022.107483.

[16] M. Zhang, C.N. Sun, X. Zhang, P.C. Goh, J. Wei, D. Hardacre, H. Li, High cycle fatigue life prediction of laser additive manufactured stainless steel: a machine learning approach, Int. J. Fatigue 128 (2019) 105194, https://doi.org/10.1016/J.IJFATIGUE.2019.105194.

[17] A. Ciampaglia, A. Tridello, D.S. Paolino, F. Berto, Data driven method for predicting the effect of process parameters on the fatigue response of additive manufactured AlSi10Mg parts, Int. J. Fatigue 170 (2023) 107500, https://doi.org/10.1016/J.IJFATIGUE.2023.107500.

[18] A. Ciampaglia, A. Tridello, F. Berto, D. Paolino, Data-driven method to assess the influence of process parameters on the fatigue response of additively manufactured Ti6Al4V, Procedia Struct. Integrity 47 (2023) 56–69, https://doi.org/10.1016/j.prostr.2023.06.041.

[19] E. Salvati, A. Tognan, L. Laurenti, M. Pelegatti, F. De Bona, A defect-based physics-informed machine learning framework for fatigue finite life prediction in additive manufacturing, Mater. Des. 222 (2022) 111089, https://doi.org/10.1016/J.MATDES.2022.111089.

[20] A. Tridello, C. Boursier Niutta, F. Berto, G. Qian, D.S. Paolino, Fatigue failures from defects in additive manufactured components: a statistical methodology for the analysis of the experimental results, Fatigue Fract. Eng. Mater. Struct. 44 (2021), https://doi.org/10.1111/ffe.13467.

[21] J. Chen, Y. Liu, Fatigue property prediction of additively manufactured Ti-6Al-4V using probabilistic physics-guided learning, Addit. Manuf. 39 (2021) 101876, https://doi.org/10.1016/J.ADDMA.2021.101876.

[22] Y.L. Lee, J. Pan, R. Hathaway, M. Barkey, Fatigue testing and analysis, 2005. doi: 10.1016/B978-0-7506-7719-6.X5000-3.

[23] L. Du, G. Qian, L. Zheng, Y. Hong, Influence of processing parameters of selective laser melting on high-cycle and very-high-cycle fatigue behaviour of Ti-6Al-4V, Fatigue Fract. Eng. Mater. Struct. 44 (2021), https://doi.org/10.1111/ffe.13361.

[24] M. Bakhtiarian, H. Omidvar, A. Mashhuriazar, Z. Sajuri, C.H. Gur, The effects of SLM process parameters on the relative density and hardness of austenitic stainless steel 316L, J. Mater. Res. Technol. 29 (2024), https://doi.org/10.1016/j.jmrt.2024.01.237.

[25] M. Mohseni, M.S. Sadeghi, A. Hemasian Etefagh, S.M. Nikouei, M. Khajehzadeh, The effect of selective laser melting process parameters and remelting scanning strategy on relative density and surface hardness of stainless steel 316L, Proceed. Institut. Mechan. Eng., Part e: J. Process Mechan. Eng. (2023), https://doi.org/10.1177/09544089231207809.

[26] J.M. Alegre, A. Díaz, R. García, L.B. Peral, I.I. Cuesta, Effect of HIP post-processing at 850 °C/200 MPa in the fatigue behavior of Ti-6Al-4V alloy fabricated by Selective Laser Melting, Int. J. Fatigue 163 (2022) 107097, https://doi.org/10.1016/J.IJFATIGUE.2022.107097.

[27] A.B. Spierings, T.L. Starr, K. Wegener, Fatigue performance of additive manufactured metallic parts, Rapid Prototyp. J. 19 (2013), https://doi.org/10.1108/13552541311302932.

[28] R. Shrestha, J. Simsiriwong, N. Shamsaei, Fatigue behavior of additive manufactured 316L stainless steel parts: effects of layer orientation and surface roughness, Addit. Manuf. 28 (2019), https://doi.org/10.1016/j.addma.2019.04.011.

[29] F. Stern, L. Becker, C. Cui, J. Tenkamp, V. Uhlenwinkel, M. Steinbacher, J. Boes, J. Lentz, R. Fechte-Heinen, S. Weber, F. Walther, Improving the defect tolerance of PBF-LB/M processed 316L steel by increasing the nitrogen content, Adv. Eng. Mater. 25 (2023), https://doi.org/10.1002/adem.202200751.

[30] W.J. Lai, A. Ojha, Z. Li, C. Engler-Pinto, X. Su, Effect of residual stress on fatigue strength of 316L stainless steel produced by laser powder bed fusion process, Prog. Addit. Manuf. 6 (2021), https://doi.org/10.1007/s40964-021-00164-8.

[31] P. Kumar, R. Jayaraj, J. Suryawanshi, U.R. Satwik, J. McKinnell, U. Ramamurty, Fatigue strength of additively manufactured 316L austenitic stainless steel, Acta Mater. 199 (2020), https://doi.org/10.1016/j.actamat.2020.08.033.

[32] G.S. Ponticelli, R. Panciroli, S. Venettacci, F. Tagliaferri, S. Guarino, Experimental investigation on the fatigue behavior of laser powder bed fused 316L stainless steel, CIRP J. Manuf. Sci. Technol. 38 (2022), https://doi.org/10.1016/j.cirpj.2022.07.007.

[33] R. Shrestha, J. Simsiriwong, N. Shamsaei, Fatigue behavior of additive manufactured 316L stainless steel under axial versus rotating-bending loading: synergistic effects of stress gradient, surface roughness, and volumetric defects, Int. J. Fatigue 144 (2021), https://doi.org/10.1016/j.ijfatigue.2020.106063.

[34] D. Kotzem, S. Kleszczynski, F. Stern, A. Elspaß, J. Tenkamp, G. Witt, F. Walther, Impact of single structural voids on fatigue properties of AISI 316L manufactured by laser powder bed fusion, Int. J. Fatigue 148 (2021), https://doi.org/10.1016/j.ijfatigue.2021.106207.

[35] X. Liang, A. Hor, C. Robert, M. Salem, F. Lin, F. Morel, High cycle fatigue behavior of 316L steel fabricated by laser powder bed fusion: Effects of surface defect and loading mode, Int. J. Fatigue 160 (2022), https://doi.org/10.1016/j.ijfatigue.2022.106843.

[36] F. Zeng, Y. Yang, G. Qian, Fatigue properties and S-N curve estimating of 316L stainless steel prepared by SLM, Int. J. Fatigue 162 (2022), https://doi.org/10.1016/j.ijfatigue.2022.106946.

[37] J. Nafar Dastgerdi, O. Jaberi, H. Remes, Influence of internal and surface defects on the fatigue performance of additively manufactured stainless steel 316L, Int J Fatigue 163 (2022), https://doi.org/10.1016/j.ijfatigue.2022.107025.
[38] C. Yu, P. Zhang, Z. Zhang, W. Liu, Microstructure and fatigue behavior of laser-powder bed fusion austenitic stainless steel, J. Mater. Sci. Technol. 46 (2020), https://doi.org/10.1016/j.jmst.2019.08.047.
[39] L. Cui, D. Deng, F. Jiang, R.L. Peng, T. Xin, R.T. Mousavian, Z. Yang, J. Moverare, Superior low cycle fatigue property from cell structures in additively manufactured 316L stainless steel, J. Mater. Sci. Technol. 111 (2022), https://doi.org/10.1016/j.jmst.2021.10.006.
[40] K. Malekipour, M. Mashayekhi, M. Badrossamay, Meso-scale damage mechanics modeling for high cycle fatigue behavior of additively manufactured components, Mech. Mater. 160 (2021), https://doi.org/10.1016/j.mechmat.2021.103951.
[41] K. Solberg, S. Guan, N. Razavi, T. Welo, K.C. Chan, F. Berto, Fatigue of additively manufactured 316L stainless steel: the influence of porosity and surface roughness, Fatigue Fract. Eng. Mater. Struct. 42 (2019), https://doi.org/10.1111/ffe.13077.
[42] E. Uhlmann, C. Fleck, G. Gerlitzky, F. Faltin, Dynamical fatigue behavior of additive manufactured products for a fundamental life cycle approach, Procedia CIRP (2017), https://doi.org/10.1016/j.procir.2016.11.138.
[43] B. Voloskov, S. Evlashin, S. Dagesyan, S. Abaimov, I. Akhatov, I. Sergeichev, Very high cycle fatigue behavior of additively manufactured 316L stainless steel, Materials 13 (2020), https://doi.org/10.3390/ma13153293.
[44] D.S. Paolino, G. Chiandussi, M. Rossetto, A unified statistical model for S-N fatigue curves: probabilistic definition, Fatigue Fract. Eng. Mater. Struct. 36 (2013), https://doi.org/10.1111/j.1460-2695.2012.01711.x.
[45] M. Raissi, P. Perdikaris, G.E. Karniadakis, Physics-informed neural networks: a deep learning framework for solving forward and inverse problems involving nonlinear partial differential equations, J. Comput. Phys. 378 (2019) 686–707, https://doi.org/10.1016/J.JCP.2018.10.045.
[46] G.E. Hinton, D. van Camp, Keeping neural networks simple by minimizing the description length of the weights, in: 1993. doi: 10.1145/168304.168306.
[47] C. Blundell, J. Cornebise, K. Kavukcuoglu, D. Wierstra, Weight uncertainty in neural networks, in: 32nd International Conference on Machine Learning, ICML 2015, 2015.
[48] X. Ying, An Overview of Overfitting and its Solutions, J. Phys. Conf. Ser. (2019), https://doi.org/10.1088/1742-6596/1168/2/022022.
[49] L. Prechelt, Early stopping - But when?, Lecture Notes in Computer Science (Including Subseries Lecture Notes in Artificial Intelligence and Lecture Notes in Bioinformatics) 7700 LECTURE NO (2012). doi: 10.1007/978-3-642-35289-8_5.
[50] B. Blinn, M. Klein, C. Gläßner, M. Smaga, J.C. Aurich, T. Beck, An investigation of the microstructure and fatigue behavior of additively manufactured AISI 316L stainless steel with regard to the influence of heat treatment, Metals (basel) 8 (2018), https://doi.org/10.3390/met8040220.
[51] P.M. Cerezo, J.A. Aguilera, A. Garcia-Gonzalez, P. Lopez-Crespo, Influence of porosity on fatigue behaviour of 18Ni300 steel SLM CT specimens at various angles, Materials 17 (2024), https://doi.org/10.3390/ma17020432.
[52] N. Sanaei, A. Fatemi, Defects in additive manufactured metals and their effect on fatigue performance: a state-of-the-art review, Prog. Mater Sci. 117 (2021), https://doi.org/10.1016/j.pmatsci.2020.100724.
[53] G. Kasperovich, J. Hausmann, Improvement of fatigue resistance and ductility of TiAl6V4 processed by selective laser melting, J. Mater. Process. Technol. 220 (2015), https://doi.org/10.1016/j.jmatprotec.2015.01.025.
[54] G. Kasperovich, J. Haubrich, J. Gussone, G. Requena, Correlation between porosity and processing parameters in TiAl6V4 produced by selective laser melting, Mater. Des. 105 (2016), https://doi.org/10.1016/j.matdes.2016.05.070.